

Jim Gw -

BNL-50321

ROTATING FLUIDIZED BED REACTOR FOR SPACE NUCLEAR PROPULSION

Annual Report:
Design Studies and Experimental Results,
June, 1970 - June, 1971



August, 1971

ENGINEERING DIVISION, DEPARTMENT OF APPLIED SCIENCE
BROOKHAVEN NATIONAL LABORATORY, ASSOCIATED UNIVERSITIES, INC.
UPTON, NEW YORK 11973

prepared for
SPACE NUCLEAR SYSTEMS OFFICE
a joint office of the
UNITED STATES ATOMIC ENERGY COMMISSION
and the
NATIONAL AERONAUTICS AND SPACE ADMINISTRATION
WASHINGTON, D.C. 20545
under
NASA AGREEMENT NO. 13254

(NASA-CR-126738) ROTATING FLUIDIZED BED
REACTOR FOR SPACE NUCLEAR PROPULSION,
ANNUAL REPORT: DESIGN STUDIES AND
EXPERIMENTAL RESULTS, (Brookhaven National
Lab.) Aug. 1971 97 p
CSCL 181 G3/22
Unclas
30526
N72-25611



**ROTATING FLUIDIZED BED REACTOR
FOR
SPACE NUCLEAR PROPULSION**

**Annual Report:
Design Studies and Experimental Results,
June, 1970 - June, 1971**

ENGINEERING DIVISION, DEPARTMENT OF APPLIED SCIENCE

CONTRIBUTORS:

J.M. HENDRIE	H. LUDEWIG
K.C. HOFFMAN	A.J. MANNING
R.J. ISLER	C.J. RASEMAN
G.C. LINDAUER	

**BROOKHAVEN NATIONAL LABORATORY, ASSOCIATED UNIVERSITIES, INC.
UPTON, NEW YORK 11973**

prepared for

**SPACE NUCLEAR SYSTEMS OFFICE
a joint office of the
UNITED STATES ATOMIC ENERGY COMMISSION
and the
NATIONAL AERONAUTICS AND SPACE ADMINISTRATION
WASHINGTON, D.C. 20545
under
NASA AGREEMENT NO. 13254**

NOTICE

This report was prepared as an account of work sponsored by the United States Government. Neither the United States nor the United States Atomic Energy Commission, nor any of their employees, nor any of their contractors, subcontractors, or their employees, makes any warranty, express or implied, or assumes any legal liability or responsibility for the accuracy, completeness or usefulness of any information, apparatus, product or process disclosed, or represents that its use would not infringe privately owned rights.

Printed in the United States of America
Available from
National Technical Information Service
U.S. Department of Commerce
5285 Port Royal Road
Springfield, Virginia 22151
Price: Printed Copy \$3.00; Microfiche \$0.95

November 1971

500 copies

PRECEDING PAGE BLANK NOT FILMED

ACKNOWLEDGMENT

The authors wish to acknowledge the guidance they received from Captain Charles E. Franklin and David J. Miller of the Space Nuclear Propulsion Office, U.S. Atomic Energy Commission. We also wish to thank W. J. Johnson and G. A. Schoener for their help in preparing special equipment. Special thanks go to C. Brewster and W. Kalinowski for construction and operating competence. We are also grateful for the design efforts of S. J. Majeski.

We are indebted to the late Jack Chernick for his stimulating discussions and guidance in the analytical aspects of this project.

CONTENTS

	Page
I. Summary	1
II. Introduction	2
III. Background and History	4
IV. Progress During Report Period	9
A. Analysis and Design	9
1. Physics	9
2. Engineering	13
B. Experimental Program	19
1. Introduction	19
2. System	19
3. Photographic Techniques	22
4. Pressure and Flow Measure- ments	23
5. Experimental Results	25
V. Future Program	30
VI. References	35
VII. Nomenclature	37

CONTENTS--Continued

List of Tables

Table		Page
I	System performance for ^{235}U - and ^{233}U - fueled engines	39
II	Fluidized bed parameters for ^{235}U system	40
III	Fluidized bed parameters for ^{233}U system	41
IV	Component weights for ^{235}U and ^{233}U systems	42

List of Figures

Figure		Page
1	Simple fluidized bed in 1-g field	43
2	Rotating fluidized bed in a multiple g field	43
3	Correlation of particulate fluidization data	44
4	Rotating fluidized bed reactor	45
5	Section through rotating fluidized bed reactor	45
6	Graph of ^{235}U and ^{233}U system parameters	46
7	Variation of thrust-to-weight ratio with thrust	47
8	Gas distribution shell showing two inlet ports and photographic access port	48
9	Inside view of shell showing gas distribu- tion baffles	49

CONTENTS--Continued

Figure		Page
10	View of rotating drum showing perforated frit support	50
11	Rotating fluidized bed assembly	51
12	Experimental facility, view from the east	52
13	Control console	53
14	Flow diagram	54
15	6,800 liter LN ₂ storage trailer	55
16	Liquid nitrogen vaporizer	56
17	High pressure nitrogen gas storage trailers	57
18a	Bottom view of rotating drum showing photographic view windows	58
18b	Inside view of rotating drum showing grid lines on viewing windows	59
19	Schematic diagram of photographic system	60
20	View of bed taken through bottom plate, Series 1-1 100 μ glass, 1,000 rpm, 0 m ³ /min	61
21	View of bed taken through bottom plate, Series 1-2 100 μ glass, 1,000 rpm, 38 m ³ /min	62
22	View of bed taken through bottom plate, Series 1-3 100 μ glass, 1,000 rpm, 45 m ³ /min	63
23	View of bed taken through bottom plate, Series 1-4 100 μ glass, 1,000 rpm, 51 m ³ /min	64

CONTENTS--Continued

Figure		Page
24	View of bed taken from bottom plate, Series 2-1 100 μ glass, 2,000 rpm, 0 m ³ /min	65
25	View of bed taken from bottom plate, Series 2-2 100 μ glass, 2,000 rpm, 63 m ³ /min	66
26	View of bed taken from bottom plate, Series 2-3 100 μ glass, 2,000 rpm, 74 m ³ /min	67
27	View of bed taken from bottom plate, Series 2-4 100 μ glass, 2,000 rpm, 82 m ³ /min	68
28	View of bed taken through bottom plate, Series 3-1 500 μ glass, 1,000 rpm, 0 m ³ /min	69
29	View of bed taken through bottom plate, Series 3-2 500 μ glass, 1,000 rpm, 85 m ³ /min	70
30	View of bed taken through bottom plate, Series 3-3 500 μ glass, 1,000 rpm, 170 m ³ /min	71
31	View of bed taken through bottom plate, Series 3-4 500 μ glass, 1,000 rpm, 213 m ³ /min	72
32	View of bed taken through bottom plate, Series 4-1 500 μ glass, 2,000 rpm, 0 m ³ /min	73
33	View of bed taken through bottom plate, Series 4-2 500 μ glass, 2,000 rpm, 85 m ³ /min	74

CONTENTS--Continued

Figure		Page
34	View of bed taken through bottom plate, Series 4-3 500 μ glass, 2,000 rpm, 170 m ³ /min	75
35	View of bed taken through bottom plate, Series 5-1 500 μ copper, 700 rpm, 0 m ³ /min	76
36	View of bed taken through bottom plate, Series 5-2 500 μ copper, 700 rpm, 170 m ³ /min	77
37	View of bed taken through bottom plate, Series 5-3 500 μ copper, 700 rpm, 232 m ³ /min	78
38	Total pressure drop per unit bed thick- ness as a function of flow rate	79
39	Frit pressure drop as a function of flow rate (1,000 rpm)	80
40	Effect of distance from closed end of bowl on pressure drop	81
41	Flow streamlines in bowl	82

I. SUMMARY

@ADS The rotating fluidized bed reactor concept is being investigated for possible application in nuclear propulsion systems. Physics calculations show ^{233}U to be superior to ^{235}U as a fuel for a cavity reactor of this type. Preliminary estimates of the effect of hydrogen in the reactor, reflector material, and power peaking are given. A preliminary engineering analysis has been made for ^{235}U and ^{233}U fueled systems. An evaluation of the parameters affecting the design of the system is given, along with the thrust-to-weight ratios.

The experimental equipment is described, as are the special photographic techniques and procedures. Characteristics of the fluidized bed and experimental results are given, including photographic evidence of bed fluidization at high rotational velocities.

@A DA Author

II. INTRODUCTION

The rotating fluidized bed reactor was initially proposed for rocket propulsion by L. P. Hatch, W. H. Regan, and J. R. Powell at Brookhaven National Laboratory in 1960.^(1,2) The fuel in this system is in the form of small diameter particles that are retained by centrifugal force in a rotating cylindrical structure to form an annular core. The use of small fluidized particles for the reactor fuel offers the following specific advantages:

1. The large surface-to-volume ratio of the fuel and the high fuel-to-coolant heat transfer coefficient permits very high rates of heat transfer with a minimum temperature difference between the fuel and gas stream.
2. Since the primary structure remains cool, design requirements are dictated by high temperature stability of the fuel rather than structural factors which are limiting in conventional solid fuel element nuclear propulsion systems.
3. The volume and mass of material that must be handled in loading and unloading fuel is less than that handled in comparable solid fuel element systems and refueling of the core is simplified.

4. The fuel particles are retained in the core by centrifugal force and the fuel loss problems that are characteristic of gas core concepts are minimized.

Thus, the rotating fluidized bed reactor promises to avoid many of the problems that limit the performance and suitability of solid fuel elements and gas core systems. High gas temperatures and a high specific impulse can be achieved, with the limit dependent on fuel particle melting and sintering properties.

III. BACKGROUND AND HISTORY

During the past several decades an extensive development effort has been made in the application of various solids-handling techniques in the chemical process industries. In the early stages of development, the fluidized bed technique displayed a number of unique advantages in (1) temperature control, (2) continuity of operation, (3) heat transfer, and (4) catalysis. Studies of the characteristics of powder suspensions (100 to 500 μ) showed that a dense concentration of solids could be maintained in a highly turbulent state by a proper combination of gas velocity and particle size of the powder. The solids appear to be buoyed up by the upflowing gas and thus exhibit a "fluid" behavior. The effective slippage between gas and solids is so great that a powder, whose particle size is small enough to exhibit a free-fall velocity of the order of 0.03 m/sec (0.1 ft/sec) can be maintained as an air-suspended bed at a superficial gas velocity of the order of 0.3 m/sec (1 ft/sec). The behavior of the agitated solids indicates excellent contact between gas and solids, with a modest pressure drop equal to the weight of the bed.

Figure 1 shows a representation of a fluidized bed with the granular material uniformly dispersed under a 1-g field.

One view shows the bed in the settled state; the other view shows the bed with fluid passing upward and expanding it to a greater height. Early fluidized bed studies were carried out with liquid flow, resulting in uniform dispersion of the material. Moreover, unless the liquid is in highly turbulent motion, the top of the bed will be flat and will remain essentially stationary so long as the velocity and the viscosity of the liquid remain the same. In the gas fluidized system, however, there is a definite tendency for bubbles to form and for a portion of the gas to pass through the bed in the form of bubbles. Whether the original bubbles pass all the way through the bed, or the bubbles collapse and new ones form, is not well known, but the latter is probably a safe assumption. The question that arises in nuclear reactor design considerations, is how much of the gas passes through the bed without contacting a sufficient number of particles to maintain efficient heat transfer. To some extent heat would transfer in the form of radiation, but the main mechanism is convective transfer.

Figure 2 shows a representation of a rotating fluidized bed with the particles held in place against the inward flow-induced drag forces by means of centrifugal force. The inner vessel and particle bed are rotated. The gas enters through the

tubular shaft, then flows inward through a porous wall which serves to support the bed. With only moderate gas flow, the material becomes fluidized and redistributes itself more or less evenly over the length of the container in the pattern of a cylindrical annulus. The minimum gas velocity for fluidization and the maximum velocity allowable before particles are carried out by the gas stream are dependent on the centrifugal force acting on the particles. Therefore, by exerting greater "g forces" by means of higher rotational speed, much higher gas flow rates may be tolerated. This in turn means more effective cooling and potentially greater output.

Fluidization data are often correlated by plotting one function of the friction factor and the Reynolds number vs. another function of the friction factor and the Reynolds number. This representation is convenient, in that the ordinate is directly proportional to the gas velocity and the abscissa is directly proportional to the particle diameter, and one can immediately see the velocity range from minimum fluidization to the carry-out velocity. Figure 3 presents such a correlation of data from Zenz and Othmer.⁽³⁾ The graph was obtained by drawing averaged lines through available data for fluidized spheres. One set of lines in the grid is labeled with the Reynolds number and the other set of lines is labeled with the void fraction, ϵ .

Preliminary studies were performed at Brookhaven in the period 1962 to 1966 with rotating beds of glass particles fluidized with air to demonstrate the principles involved and to provide a basis for the definition of a development program. A rotating fluidized bed test rig with a 25.4 cm (10 in.) diameter by 2.54 cm (1 in.) long bed was operated with various bed depths at 138, 500, and 3,450 g.⁽⁴⁾ As expected, no loss of the simulated fuel occurred during these experiments and the beds did not show any instabilities.

Experiments were planned to determine the bed dynamics of a fluidized bed with a length-to-diameter ratio of 1.0. Design work was completed on a rig that would hold a 25.4 cm (10 in.) diameter by 25.4 cm (10 in.) long bed. Construction of this rig had been initiated in 1966 and several components including the rotating fluidized bed assembly were completed before work was stopped for lack of funding.

Additional experiments were performed to determine particle-to-fluid heat transfer coefficients in beds fluidized at high mass velocities.⁽⁴⁾ Although these experiments were performed in 1-g systems, the results indicated that heat transfer coefficients were well in excess of $5.68 \text{ kW/m}^2\text{-}^\circ\text{K}$ ($1,000 \text{ Btu/hr-ft}^2\text{-}^\circ\text{F}$), a value used in preliminary calculations for the rotating fluidized bed reactor system.

Computational techniques that may be applied to the thermal, mechanical, and nuclear analyses of the propulsion system are currently operational. Also available are stress codes developed at BNL, including one specifically prepared for high-speed rotating equipment and another for thermo-mechanical and shock stress analysis.

The rotating fluidized bed reactor concept is illustrated in Figures 4 and 5. The UC-ZrC particulate fuel is retained by centrifugal force in the rotating assembly which is made up of a porous metal cylinder backed up by a squirrel cage-type support structure. The hydrogen coolant passes first through cooling passages on the rocket nozzle and through the reflector region and is completely vaporized before entering the core region. The gas then flows radially inward through the cylindrical structure and annular core at a velocity sufficient to fluidize the bed. Finally, the heated gas flows out through the propulsion nozzle located at the aft end of the chamber.

IV. PROGRESS DURING REPORT PERIOD

A. Analysis and Design

1. Physics

The dependence of critical mass on cavity size was studied for a rotating fluidized bed reactor.^(5,6) Criticality determinations for these studies were based on two-dimensional transport theory and the ABBN⁽⁷⁾ cross section set for the following geometry: 0.559 m (22 in.) diameter cavity of variable length containing a 7.62 cm (3 in.) thick, 70% void, fluidized fuel annulus with a 0.254 m (10 in.) average diameter nozzle at one end of the cavity. The thickness of the Be reflector surrounding the reactor both radially and at the ends was also varied.

From these studies it was found that three to four times as much fuel was required to ensure criticality when using ^{235}U as compared with ^{233}U . The decrease in critical mass for ^{233}U is largely due to the higher value of η , the average neutron yield per neutron absorbed in fuel, for ^{233}U (2.29 vs 2.08). Furthermore, all the systems considered were required to be critical with an atom percentage of uranium in the UC-ZrC mixture of less than 10%. This is to be considered an upper limit for the uranium atom percent, since larger quantities of uranium lower the melting point of UC-ZrC to unacceptably low values.

Perturbation effects on reactivity due to fuel layer thickness, presence of hydrogen, and BeO as a reflector were also estimated. These estimates were made using a spherical geometry. It was found that changes from the original thickness have a small effect on reactivity. Furthermore, it could be concluded that the addition of hydrogen has a negative worth in the reflector and a positive worth in the core, the over-all effect being positive. Finally, it was found that BeO as a reflector would have a positive effect (~1.48%) on reactivity.

Other factors tending to increase critical mass requirements are the presence of rotating gear and the requirement for coolant channels. With a 0.305 m (12 in.) Be reflector (10% void), 0.203 m (8 in.) nozzle-throat diameter, and Zr as the rotating gear material, the critical loadings for ^{235}U - and ^{233}U -fueled reactors were determined.

In the case of the ^{233}U -fueled reactor, it was found that with a cavity length of 0.559 m (22 in.), a bed i.d. of 0.51 m (20 in.), and bed thickness of 7.62 cm (3 in.) with 70% void, a critical configuration was achieved.

These values correspond to a critical mass of 47.9 kg (105.6 lbm) UC and a uranium at.% of 7.5 in the UC-ZrC mixture, well below the 10% limit.

The ^{235}U system required a cavity length of 0.635 m (25 in.), a bed i.d. of 0.635 m (25 in.), and a fuel bed depth of 0.102 m (4 in.) with 60% void. The corresponding critical mass is 155.8 kg (343.5 lbm) UC and uranium at.% of 9.5% in the UC-ZrC mixture. The following conclusions can be drawn from this study:

- a. Uranium-233 has a clear advantage over ^{235}U as a fuel for a cavity reactor to be used for rocket propulsion. This advantage can be utilized either in reducing the weight of the rocket motor, or reducing the uranium at. % in the UC-ZrC mixture. The reduced weight implies a better thrust-to-weight ratio and the reduced uranium at. % implies a higher fuel melting temperature. A higher melting temperature makes it possible to have a higher specific impulse. Finally, a reduced loading of uranium has the effect of lowering the peak-to-average power ratio and thus leads to a more uniform temperature distribution within the bed.
- b. The effect of hydrogen in the reactor is estimated to be positive. This estimate will have to be refined to allow for the temperature change in the hydrogen as it passes from the cooler parts of the reflector to the center of the cavity.

- c. Replacing the beryllium in the reflector with beryllium oxide has a slight positive effect on the reactivity. However, due to its relatively high density it would be impractical to construct the entire reflector of BeO. It might be useful, though, to line the inside of the reflector with a layer of BeO since it can withstand the high temperatures expected in this region. In the cooler outside of the reflector, Be metal could then be used to minimize the weight.
- d. The axial power peaking found⁽⁸⁾ in the hypothetical system is reduced in the realistic case, since the rotating gear and larger nozzle opening act as poisons. Artificial poisons can still be added, as suggested in reference 8, to flatten out any undesirable axial peaking.
- e. The radial power peaking is also reduced in the realistic cases because of the presence of the rotating gear. In the case of the radial power variation, the peak occurs at the outer boundary, which is characteristic of reflector-moderated reactors.⁽⁹⁾ The peak-to-average in the radial direction is of the order of 2:1; however, it is a function of the type

of fuel, as pointed out under (a). The thermal effect on the fuel bed, due to this comparatively high peak-to-average power density, however, is reduced somewhat because the coolest propellant is in contact with that part of the fuel bed experiencing the power peak.

2. Engineering

In this section the operating conditions for two rotating fluidized bed rocket reactors are presented. The two systems considered are based on criticality calculations⁽⁶⁾ for ^{233}U - and ^{235}U -fueled reactors. In summary, the physical sizes of these systems are:

- a. For the ^{233}U -fueled reactor, it was found that with a cavity length of 0.56 m (22 in.), a bed i.d. of 0.51 m (20 in.), and a bed thickness of 0.0762 m (3 in.) with 70% void, a critical configuration was achieved. These values correspond to a critical mass of 47.9 kg (105.6 lb m) UC and a uranium at. % of 7.5 in the UC-ZrC mixture.
- b. The ^{235}U system required a cavity length of 0.635 m (25 in.), a bed i.d. of 0.635 m (25 in.), and a fuel bed depth of 10.2 cm (4 in.) with 60% void. The

corresponding critical mass is 155.8 kg (343.5 lbm) UC, implying a uranium at. % of 9.5 in the UC-ZrC mixture.

Both the above systems had reflectors of beryllium 0.305 m (12 in.) thick, reduced in density by 10% to allow for propellant ducting, and a nozzle throat diameter of 17.78 cm (7 in.).

In the analysis which follows, it is assumed that the cavity operating pressure is allowed to vary from 5.17 MN/m^2 (750 psia) to 41 MN/m^2 (6,000 psia) in five steps. At every value of the pressure, two temperatures, $3,400^\circ \text{K}$ ($6,120^\circ \text{R}$) and $2,361^\circ \text{K}$ ($4,250^\circ \text{R}$), are assumed. The specific impulse, power, thrust, and propellant flow rate were determined for the ten cases described above, and are tabulated in Table I. In the determination of the specific impulse, an adiabatic isentropic expansion with a pressure ratio of 10,000:1 was assumed.

An estimate of the fuel particle size and thermal stress, drum speed, and pressure drop across the bed was made next, for the two systems considered. In making these estimates it was assumed that the bed void factor at the bed exit was 0.75. For hydrogen, at the above temperature

and pressures, and for the fuel density involved, the following relationship was assumed: (3)

$$\frac{D_p}{\left[\frac{3}{4} \frac{\mu_f^2}{\rho_f (\rho_p - \rho_f) g} \right]^{1/3}} = 15.0 \frac{V_e}{\left[\frac{4}{3} \frac{\mu_f (\rho_p - \rho_f) g}{\rho_f^2} \right]^{1/3}}$$

Here D_p and ρ_p are the particle diameter and density; μ_f and ρ_f , the fluid viscosity and density; and V_e is the superficial fluid velocity through the bed. Thus, for a given particle size, D_p , the value of g (radial acceleration) may be determined, from which the rotational speed of the bed and the pressure drop across the bed may be computed. On the other hand, for a given pressure drop a corresponding particle size may be determined. With a knowledge of the power generated and the particle size, it is possible to compute the thermal stress, assuming a spherical particle.

Tabulated on Tables II and III are four of the parameters mentioned above for the two reactors under consideration. For each reactor two choices of constant particle diameter were considered, 100 and 400 μ , and one case of a constant pressure drop of 2.8 MN/m² (400 psia) and a variable particle diameter.

Finally, an estimate of the thrust-to-weight ratio of these systems was made. The total weight of the rocket engine was assumed to be made up of the following components:

- a. fixed weight, including reflector, nuclear fuel, and rotating gear,
- b. nozzle and controls,
- c. pressure vessel, and
- d. turbopump for propellant feed.

The fixed weight was determined by the criticality calculation for the reactor, which determines the fuel loading, reflector thickness, and cavity size. Weights for the nozzle and control systems were obtained by extrapolation and interpolation of published data.⁽¹¹⁾ Data for the weight of the converging section of the nozzle are given as a function of reactor outer diameter for a given cavity pressure. In order to obtain the variation of convergent section weight with cavity pressure for a given reactor, these data were cross plotted, and the curves corresponding to the two reactors considered are shown in Figure 6 and labeled (a) and (b). In the case of the turbopump and the divergent section of the nozzle, the data are presented as the variation of weight with flow rate (\dot{M}) for various cavity pressures. In this

case, the gradients of each of these curves, which happen to be linear, were determined for each cavity pressure. These gradients were then plotted against cavity pressure and thus the gradients corresponding to any cavity pressure of interest, can be found. The curves labeled (c) and (d) on Figure 6 are the variation of gradient with cavity pressure for the divergent section and turbopump, respectively. The weight of either the turbopump or divergent nozzle section for a given cavity pressure is thus obtained by multiplying the corresponding gradient by the mass flow rate for the system of interest. Finally, the pressure vessel weight was estimated by determining its thickness, computing the volume of materials involved and thus the weight. The thickness was determined using the thin cylinder formula and allowing for a stress of 690 MN/m^2 (100,000 psi). The results of this study are tabulated in Table IV for both reactors. Figure 7 shows the variation of thrust-to-weight ratio with thrust for the two systems considered.

The conclusions of this study are as follows:

- a. It can be seen from Tables II and III that for any real system a compromise must be struck between particle size and pressure drop across the bed. Small particles result in low thermal stresses but require

high rotational speeds and thus imply high centrifugal stresses in the rotating gear. Larger particles suffer severe thermal stresses, but since the required rotational speed is lower, the centrifugal stress problem is not as severe.

- b. From Table IV it can be seen that a large proportion of the total weight of a rocket engine is in the fixed weight, especially for the low thrust systems. Thus, to minimize the weight of any system it is important to minimize the reflector weight. The way to achieve a minimum reflector weight is to minimize the loss of neutrons in the structural material due to absorption and streaming out of the nozzle. Since the loss due to absorption cannot be varied a great deal, the nozzle throat area should be minimized for a given thrust level in order to minimize the weight for an optimum design. It appears from the positions of the maxima in Figure 7 that the 17.78 cm (7 in.) nozzle throat diameter used throughout the parametric studies is near optimum for a thrust level of ≈ 1.5 MN (330,000 lb).

B. Experimental Program

1. Introduction

A major problem to be investigated in the development of a rotating fluidized bed reactor is the uniformity of distribution of the fuel particles in the gas coolant.

Currently, an experimental program is in progress to investigate whether bed length-to-diameter ratio affects the uniformity of fuel particle distribution. The primary effort, to date, has been associated with the activation of a 0.254 m (10 in.) by 0.254 m (10 in.) diameter rotating fluidized bed.

2. System

The construction of the rotating bed equipment and piping system is completed and the apparatus is assembled in its permanent location in BNL Building 835. Figures 8 through 13 show the apparatus. Figure 8 shows the stationary housing of the test bed, prior to assembly of gas piping and other equipment. Figure 9 is a view looking down into the empty housing. Figure 10 shows the rotating assembly which fits within the housing. The perforated, ribbed aluminum cylinder is the strength member of the rotating bed wall. A porous frit layer inside the aluminum section prevents the small particles of the bed from escaping

outward during periods of rotation without gas flow, and distributes the gas uniformly around the cylinder during gas flow. The top opening in the rotating assembly is the gas exit nozzle. Pulleys at the bottom of the assembly take V-belts from the driving motor.

Figure 11 shows the bed assembly, with driving motor to the left and gas supply piping attached to the bed stationary housing. Figure 12 shows the bed assembly and interior of the test bay. Figure 13 shows the control and data panels for the experiment. The flow diagram of the system is illustrated in Figure 14.

The apparatus is instrumented to measure the gas temperature and pressure in the manifold, at the orifice, and in the inlet, as well as the gas flow rate. There is also a pitot tube to measure the pressure drop across the bed. The fluidizing gas is nitrogen from a recharging system capable of delivering $\approx 16,700$ STP m^3/h (10,000 scfm).

Nitrogen was chosen for the experiments because of its ready availability, low cost, and because it is a reasonably good match, at the pressures and temperatures used in the experiments, to the high pressure, high temperature hydrogen of the reactor. Liquid nitrogen is obtained from local commercial sources and is stored in the

experimental area in a trailer-mounted 6,800 liter (1,800 gal) Dewar, shown in Figure 15. The liquid nitrogen is pumped to 16.6 MN/m^2 (2,400 psig) pressure and is piped to the unit shown in Figure 16, where it is vaporized. The high pressure gas is stored in two storage trailers until needed. The storage trailers, shown in Figure 17, have a total capacity of $2,260 \text{ STP m}^3$ at 16.6 MN/m^2 (80,000 scf at 2,400 psig). A third trailer is available but has not been as yet connected to the manifold system.

The following procedure is used in performing experiments:

- a. The orifice plate required for the range of flow rates to be used is installed.
- b. The desired weight of particles is loaded into the cylinder.
- c. The cylinder is rotated at 500 rpm.
- d. The 0.1 m (4 in.) line is filled with N_2 at 0.79 MN/m^2 (100 psig) up to the block valve.
- e. The throttle valve is opened completely and then the block valve is opened. The resulting gas flow fluidizes the bed.
- f. The bed is rotated at 1,000 rpm.

- g. Steps d and e are repeated with N_2 pressure $\approx 1.13 \text{ MN/m}^2$ (150 psig).
- h. The two pressure regulators are set at their desired values.
- i. The cylinder rotation is increased to the desired value for the experimental run.
- j. The bed is refluidized at this rotational speed.
- k. Flow is increased through the preselected range; photographs and measurements of temperature, pressure, and flow are taken at selected points.

3. Photographic Techniques

One of the objectives of the experiment is to determine the dynamic behavior of the rotating fluidized bed. Photographic techniques are being utilized for this purpose. The bed apparatus is arranged so that single frame photographs may be taken through windows in the bottom plate of the rotating assembly. Figure 18a shows the rotating assembly (with drive pulleys removed) in an inverted position. The two windows for photography appear on opposite sides of the drive shaft hub. Figure 18b is a view looking down into the rotating assembly from the top. The bottom plate of the assembly is flat, with circular fiducial marks scored at 0.317 cm (.125 in.) radial intervals. Figure 19 is a schematic

drawing of the photographic system using the windows in the assembly bottom plate.

The view in photographs of bed behavior (see Figures 20, 21, etc.) is thus looking upward at the bottom of the bed, with the lower surface of the bed in relatively sharp focus. The view is actually slightly inclined outward from a point below and inside the inner radius of the bed, so that a portion of the bed inside vertical surface can be seen. Illumination is by a synchronized light flash from outside the assembly. Due to limitations on the light source, consecutive photographs must be at least five seconds apart.

4. Pressure and Flow Measurements

The available locations for pressure measurements on the rotating fluidized bed are the annular space between the stationary housing and the rotating assembly, where a static tap gives the upstream pressure, and the cylindrical cavity within the rotating bed. A pitot tube in the cavity gives the pressure downstream of the bed.

The total pressure drop between these measurement points has three components. The first is the pressure drop through the porous frit layer of the rotating assembly. This component can be measured as a function of rotational

speed and gas flow rate by operating the apparatus with no particles in the cavity. The first measurements of this component were made toward the end of the report period and are discussed in the next section.

The second component of the total pressure drop is the drop through the expanded bed itself. It is obtained by subtracting the first and third components from the observed total pressure drop. The third component is the pressure drop from the free surface of the expanded bed to the downstream measurement point. This component is a function of the gas flow rate and pitot tube location within the cavity. It can be determined by mapping the pressure drop pattern within the cavity. A first set of measurements of this kind are reported in the next section.

The gas flow rate is determined by measuring the pressure drop across one of a set of calibrated orifice plates. The plates are sized so that maximum flow through a plate yields a pressure drop of 99.5 kN/m^2 (400 in. water gauge) for the gas reference conditions in the supply manifold of 1.13 MN/m^2 (150 psig) pressure and 273°K (32°F) temperature. Flow rates for any particular upstream pressure and temperature and any pressure drop across the orifice can be obtained by applying standard corrections.

5. Experimental Results

Experiments with 100 μ glass spheres have been performed at 1,000 rpm (140 g) and 2,000 rpm (560 g). Photographs taken during operation indicate that fluidization was obtained during each of the runs with gas flow. Figures 20 through 27 show some of the photographs obtained in this series of experiments. Note that the "haze" of particles which appears to be rising inboard of the inner surface of the bed is actually the vertical surface of the bed, and appears in the photographs because of the slight inclination of the line of sight. This visual effect is quite apparent in Figures 20 and 24, taken with no gas flow and the particle bed fully settled against the frit wall in each case.

The extent of fluidization varied from an expanded annular bed without visible surface particle fluctuations to an annular bed with severe surface eruptions, depending on the flow rate used. The range of flow rates was from 38 to 51 STP m^3/min (1,340 to 1,800 scfm). No particle loss was observed. It can be seen from the photographs that less bubbling occurred at 2,000 rpm and the bed expansion was reduced.

Experiments were also performed with 500 μ glass spheres. For the experiments at 140 g, flow rates were varied from 63 to 240 STP m^3/min (2,225 to 8,475 scfm) (Figures 28 to 31). At the lower flow rates, the bed was slightly expanded and essentially annular without marked surface fluctuations. At the highest flow rate, eruptions occurred that at times resulted in particles being projected 1.9 cm (0.75 in.) from the porous wall. At the conclusion of the run it was determined that no particle loss from the bed had occurred.

At 560 g, flow rates were varied from 68 to 240 STP m^3/min (2,400 to 8,475 scfm) (Figures 32 to 34). Although bed expansion and fluidization occurred at higher flow rates, the bed remained essentially annular and smooth-surfaced throughout.

Further experiments were performed with copper particles, $\approx 500 \mu$ in diameter. The bed containing copper particles was operated at 1,500 rpm (315 g), 1,000 rpm (140 g), and 700 rpm (69 g) to determine the capabilities of the system for fluidizing higher density particles. Calculations based on modification of 1-g fluidizing correlations for high g values indicated that complete fluidization would not be obtainable at 1,000 rpm (due to flow

rate limitations), but would be obtainable at 700 rpm. The experiments confirmed this result (Figures 35 to 37). Similar calculations were performed to estimate the flow rate required to fluidize these particles at 2,000 rpm (560 g). The result, between 566 and 708 m³/min (20,000 and 25,000 scfm), is beyond the capabilities of the present system. New equipment that will provide substantially greater flow rates is on order.

In the early fluidization experiments pressure taps were not placed to measure system pressure drop. Data taken after the upstream and downstream taps were installed are shown in Figure 38. Figure 38 shows a representative plot of total pressure drop vs gas flow rate for several sets of conditions. It should be noted that the pressure drop is expressed per unit thickness of bed, which should normalize all bed thicknesses. The point of minimum fluidization is apparent for the 500 μ glass bead runs made at 1,000 rpm. At 2,000 rpm (for 500 μ glass bead) the curve is seen to follow very closely the curve for 1,000 rpm, but continues to a higher value of minimum fluidization. The highest flow rates for the 500 μ glass at 2,000 rpm and 500 μ copper at 700 rpm were visually observed to be fluidized. This would mean that at higher flow rates these curves also would flatten out.

Experiments were performed to measure the pressure drop across the supporting frit. As noted earlier, these data are necessary to be able to determine the actual pressure drop across the bed. They also give good indications of the flow profile throughout the entire engine.

Figure 39 is a plot of pressure drop across the frit as a function of gas flow rate at a rotational speed of 1,000 rpm. Data are shown for measurements made at 6.99 cm (2.75 in.) from the frit. These data are for a constant angular velocity (1,000 rpm) and approximately constant distance from the closed end of the engine.

As noted earlier, the entire pressure drop does not occur across the frit. Due to expansion through the throat of the engine, the pressure drop changes significantly with the distance from the frit and with elevation, at high flow rates. A pressure map must be made to determine the correction for downstream measurement position. Figure 40 shows the effect of elevation above the closed end of the engine at a constant radial distance from the frit of 6.99 cm (2.75 in.). It is noted that at low flow rates there is little difference in pressure drop with elevation. This would indicate good gas distribution and uniform flow through the frit. The increase in pressure drop near the

throat of the engine at high flow rates is thought to be due to a drag contribution of the pitot tube as the flow direction changes from radial to axial in this area.

Using the pressure drop contours, the flow streamlines through the engine can be estimated. Two such streamline plots are shown in Figure 41. It is hypothesized that for low flow rates the flow is essentially radial until it reaches the central core where it becomes essentially axial. At higher flow rates, however, the streamlines deviate from the radial direction much sooner and make a smooth transition to axial flow.

V. FUTURE PROGRAM

The main effort of the report period has been to assemble the rotating bed experimental apparatus and shake down the equipment and the operating procedures. A number of experiments were run, but the measurements were of a preliminary nature in most cases. Substantial improvements in observational techniques have been under way, with some of these tested by the end of the report period. Against this background, it seems worthwhile to outline current plans for the next year.

In the physics and engineering areas, work will be done on reactivity fluctuation effects, power distributions and temperature profiles, reference design studies, and mechanical layouts. Reactivity fluctuations occur because the bed fuel density at a given point fluctuates as gas bubbles form and collapse. These density variations are random in time and space, and preliminary estimates indicate that they should not be an operational problem. It is important, however, to improve our understanding of the effects of the density, hence reactivity fluctuations on the kinetic behavior of the reactor and to define any operating limits that might be imposed by these effects. Further calculations of the reactor power distribution and the resulting temperature profiles through the bed also need to be made, with particular consideration given

to practical ways to improve the power distribution shape. The component weight scaling laws used in the parametric studies to date need to be refined since they have a dominating effect in engine optimization. Better definition of engine weight aspects, in turn, require preliminary layouts and mechanical design work.

In the experimental program area a number of improvements will be made. Improved photographic techniques are needed for observation of bed behavior. Two methods of continuous frame photography are being pursued. The first technique is an extension of the single frame photography currently in use. An available camera has been modified for pulsed operation at speeds up to fifteen frames per second. This camera will be electronically synchronized with a Strobotac light source and with the bed rotation to allow photographing the bed through one of the windows in the bottom plate. The camera will be synchronized to photograph the same section of the bed on every revolution or multiple thereof, to yield a "movie" of the bed behavior as seen through the viewing window. Preliminary tests of the illumination and photographic systems indicate that this scheme should be workable.

The second technique involves taking moving pictures through the outlet nozzle using a motion picture camera.

Photographs will be taken through a Dove prism rotating at one-half the bed speed to allow continuous viewing of one specific surface region of the bed. The system for mounting and driving the prism has been designed and is being constructed.

An important feature of these experiments is the quantitative determination of the point of minimum fluidization for rotating fluidized beds. The point of minimum fluidization can be determined from a plot of pressure drop vs. flow rate through the bed. Fluidization is achieved when there is no longer an increase in pressure drop through the bed as the flow rate is increased, i.e., the drag force on the particle equals the weight of the bed. Further increases in flow rate only cause an increased bed expansion.

As has been noted, the pressure drop across the bed is measured by placing a static pressure tap in the chamber between the bed wall and containment vessel and another downstream of the bed in the cavity. Since the pressure in the bed varies with axial and radial location, axial and radial traverses of pressure downstream of the bed must be taken. A mechanical device for performing remotely controlled axial traversing with the bed in motion is under construction. With this device in operation, pressure mapping of the bed cavity can be rapidly carried out, and the determination of the actual bed pressure drop can

be made with reasonable accuracy. This will enable correlations to be made predicting the point of complete fluidization and the lower limit of entrainment (point at which the bed particles are expelled). After the point at which complete fluidization occurs is determined, an attempt will be made to correlate the data using standard techniques developed for 1-g beds.

Experimental runs in the first few months of FY 1972 will be a continuation of the cavity pressure map measurements and of the pressure drop measurements across the supporting frit. These will cover the entire range of available flow rates and rotational speeds up to 5,000 rpm.

During the rest of the year there will be a series of bed runs covering the following parameters:

particle size:	100 and 500 μ
particle specific gravity:	2.5 to 8.9
bed thickness:	.63 to 2.5 cm
rotational speed:	1,000 to 5,000 rpm (140 to 3,450 g)

Beginning in the second quarter of FY 1972, heat transfer studies will be initiated to verify calculations on proposed heat transfer coefficients. A 1-g simulation will be examined to determine the effect of backmixing due to fluidization on the temperature profile across a bed. These experiments will

be conducted using a bed fluidized in a tube. In one case the heat will be provided by a flame front at the surface of the bed, and in the other by external, concentric induction heater coils.

VI. REFERENCES

1. Hatch, L. P., Regan, W. H., and Powell, J. R. Fluidized solids as a nuclear fuel for rocket propulsion. ARS Semi-Annu. Meet., Los Angeles, California, May 1960.
2. Hatch, L. P., Regan, W. H., and Powell, J. R. Fluidized bed for rocket propulsion. Nucleonics, 18, No. 12, 102-3, Dec. 1960.
3. Zenz, F. A. and Othmer, D. F. Fluidization and Fluid Particle Systems (Reinhold Publishing Corp., New York) 1960.
4. Lindauer, G. C., Tichler, P., and Hatch, L. P. Experimental studies on high-gravity rotating fluidized beds. Brookhaven National Laboratory, BNL-50013 (T-435), Sept. 1966.
5. Ludewig, H. and Chernick, J. Physics parameters of the Hatch reactor. Trans. Amer. Nucl. Soc., 14, 11 (1971).
6. Ludewig, H. Physics parameters for a fluidized bed cavity reactor. Internal Brookhaven National Laboratory Memorandum, June 1971.
7. Abagyn, L. P. et al. Group constants for nuclear reactor calculations. Consultants Bureau, New York, New York, 1964.

References--Continued

8. Chernick, J. Power distributions in rotating bed reactors, Internal Brookhaven National Laboratory. Memorandum to W. E. Winsche, Feb. 1970.
9. Safanov, G. Externally-moderated reactors. Proc. 2nd Geneva Conf. 12, 705 (1958).
10. Bussard, R. W. and DeLauer, R. D. Fundamentals of Nuclear Flight (McGraw Hill Book Co., New York) 1965.
11. Johnson, P. G. and Smith, R. L. Optimization of power plant parameters for orbital-launch nuclear rockets, NASA-TN-D-675 (1961).

VII. NOMENCLATURE

Btu = British thermal unit,

cm = centimeter,

C_D = drag coefficient,

D_p = particle diameter,

ft = foot,

g = gravitational constant,

h = hour,

i = variation of weight of divergent section of nozzle
with flow rate as a function of cavity pressure,

in. = inch,

I_{SP} = specific impulse,

j = variation of weight of turbopump with flow rate as
a function of cavity pressure,

kg = kilogram,

kW = kilowatt,

lbf = pound force,

lb m = pound mass,

m = meter,

\dot{M} = flow rate,

MN = meganewton,

MW = megawatt,

N = newton,

psi = lbf per inch²,
psia = lbf per inch² absolute,
psig = lbf per inch² gage,
rpm = revolutions per minute,
Re = Reynolds number,
s, sec = second,
scf = standard cubic feet,
scfm = standard cubic feet per minute,
STP = standard temperature and pressure,
 V_e = superficial fluid velocity,
°F = degrees Fahrenheit,
°K = degrees Kelvin,
°R = degrees Rankine,
 ϵ = void fraction,
 η = average neutron yield per neutron absorbed,
 μ = micron,
 μ_f = fluid viscosity,
 ρ_f = fluid density,
 ρ_p = particle density,
 σ_t = tangential thermal stress, and
 Δ_p = pressure drop.

Table I

System performance for ^{235}U - and ^{233}U -fueled engines

Case	Cavity pressure		Cavity temperature		Power MW	\dot{M} (propellant flow rate)		Thrust		I_{SP}		^{235}U -fueled Thrust/weight		^{233}U -fueled Thrust/weight	
	psia	MN/m ²	°R	°K		lb/sec	kg/sec	lbf x10 ³	kN	sec	m/sec	lbf/lbm	N/kg	lbf/lbm	N/kg
1	750	5.2	4,250	2,367	878	62.3	28.3	52	231	834.6	8,185	5.5	54	7.9	77
2	750	5.2	6,120	3,400	1,053	51.9	23.5	52	231	1,001.5	9,821	5.6	55	8.0	78
3	1,125	7.8	4,250	2,367	1,317	93.4	42.3	78	347	834.6	8,185	7.4	73	10.7	105
4	1,125	7.8	6,120	3,400	1,579	77.9	35.3	78	347	1,001.5	9,821	7.5	74	10.9	107
5	1,500	10.3	4,250	2,367	1,756	124.6	56.5	104	463	834.6	8,185	8.7	85	12.7	125
6	1,500	10.3	6,120	3,400	2,105	103.8	47.1	104	463	1,001.5	9,821	8.9	87	13.1	128
7	3,000	20.7	4,250	2,367	3,513	249.2	113.0	208	925	834.6	8,185	11.6	114	15.6	153
8	3,000	20.7	6,120	3,400	4,211	207.6	94.2	208	925	1,001.5	9,821	12.1	119	16.5	162
9	6,000	41.4	4,250	2,367	7,026	498.3	226.0	416	1,850	834.6	8,185	12.5	123	15.6	153
10	6,000	41.4	6,120	3,400	8,421	415.3	188.4	416	1,850	1,001.5	9,821	13.4	131	17.0	167

Table II
Fluidized bed parameters for ^{235}U system

rpm = revolutions per minute
 D_p = particle diameter
 Δp = pressure drop
 σ_t = tangential thermal stress

Case												
	rpm	D_p micron	Δp MN/m^2	σ_t MN/m^2	rpm	D_p micron	Δp MN/m^2	σ_t MN/m^2	rpm	D_p micron	Δp MN/m^2	σ_t MN/m^2
1	1,350	100	3.34	0.88	1,225	114	2.76	1.14	477	400	0.419	14.0
2	1,500	100	4.15	1.05	1,225	131	2.76	1.81	531	400	0.518	16.8
3	1,490	100	4.10	1.32	1,225	130	2.76	2.23	528	400	0.512	21.1
4	1,660	100	5.08	1.58	1,225	150	2.76	3.56	588	400	0.635	25.3
5	1,600	100	4.73	1.76	1,225	143	2.76	3.61	567	400	0.592	28.1
6	1,790	100	5.86	2.08	1,225	165	2.76	5.75	631	400	0.733	33.7
7	1,910	100	6.69	3.51	1,225	181	2.76	11.5	675	400	0.836	56.2
8	2,120	100	8.29	4.21	1,225	208	2.76	18.3	751	400	1.04	67.4
9	2,270	100	9.47	7.02	1,225	228	2.76	36.4	802	400	1.18	112.0
10	2,530	100	11.7	8.42	1,225	262	2.76	58.0	893	400	1.47	135.0

Table III

Fluidized bed parameters for ^{233}U system

rpm = revolutions per minute

 D_p = particle diameter Δp = pressure drop σ_t = tangential thermal stress

Case												
	rpm	D_p micron	Δp MN/m^2	σ_t MN/m^2	rpm	D_p micron	Δp MN/m^2	σ_t MN/m^2	rpm	D_p micron	Δp MN/m^2	σ_t MN/m^2
1	1,980	100	2.44	1.69	2,105	92	2.76	1.44	700	400	0.305	27.1
2	2,200	100	3.02	2.03	2,105	106	2.76	2.29	780	400	0.378	32.4
3	2,190	100	2.99	2.54	2,105	105	2.76	2.83	775	400	0.373	40.6
4	2,440	100	3.71	3.04	2,105	122	2.76	4.51	863	400	0.463	48.7
5	2,360	100	3.45	3.38	2,105	116	2.76	4.57	833	400	0.432	54.1
6	2,620	100	4.28	4.05	2,105	134	2.76	7.29	927	400	0.535	64.9
7	2,800	100	4.88	6.77	2,105	146	2.76	14.5	991	400	0.610	108.0
8	3,120	100	6.05	8.11	2,105	169	2.76	23.1	1,103	400	0.756	130.0
9	3,330	100	6.91	13.5	2,105	184	2.76	46.0	1,178	400	0.864	217.0
10	3,710	100	8.56	16.2	2,105	213	2.76	73.4	1,311	400	1.070	260.0

TABLE IV
 Component weights for ^{235}U and ^{233}U systems
 weights in kg

Case	^{235}U system					^{233}U system				
	<u>fixed weight</u>	<u>nozzle & controls</u>	<u>pressure vessel</u>	<u>turbo-pump</u>	<u>total weight</u>	<u>fixed weight</u>	<u>nozzle & controls</u>	<u>pressure vessel</u>	<u>turbo-pump</u>	<u>total weight</u>
1	3,390	420	350	110	4,270	2,320	293	260	107	2,980
2	3,390	400	350	90	4,230	2,320	280	260	90	2,950
3	3,390	595	530	235	4,750	2,320	357	390	233	3,300
4	3,390	580	530	200	4,700	2,320	340	390	200	3,250
5	3,390	770	840	410	5,410	2,320	450	520	410	3,700
6	3,390	750	840	340	5,320	2,320	430	520	340	3,610
7	3,390	1,420	1,540	1,760	8,110	2,320	910	1,050	1,760	6,040
8	3,390	1,390	1,540	1,490	7,810	2,320	880	1,050	1,470	5,720
9	3,390	2,620	2,950	6,140	15,100	2,320	1,550	2,090	6,140	12,100
10	3,390	2,580	2,950	5,180	14,100	2,320	1,510	2,090	5,180	11,100

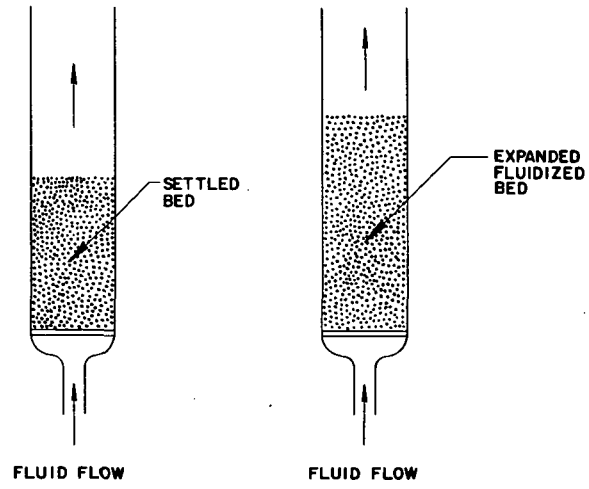


Figure 1 Simple fluidized bed in 1-g field

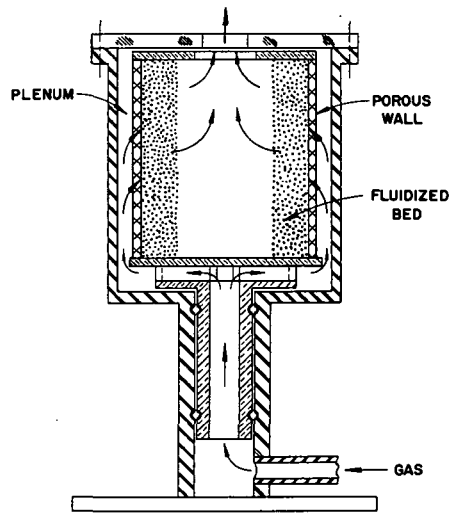


Figure 2 Rotating fluidized bed in a multiple g field

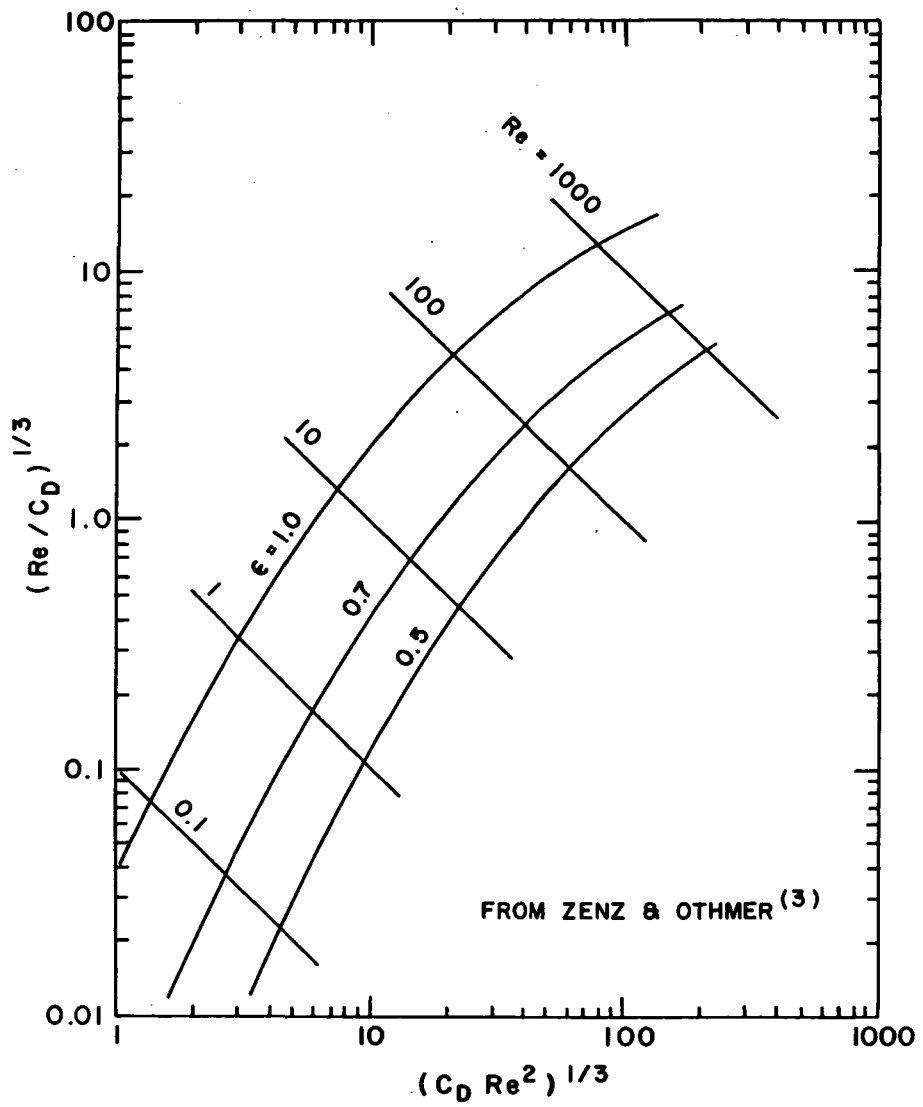


Figure 3 Correlation of particulate fluidization data

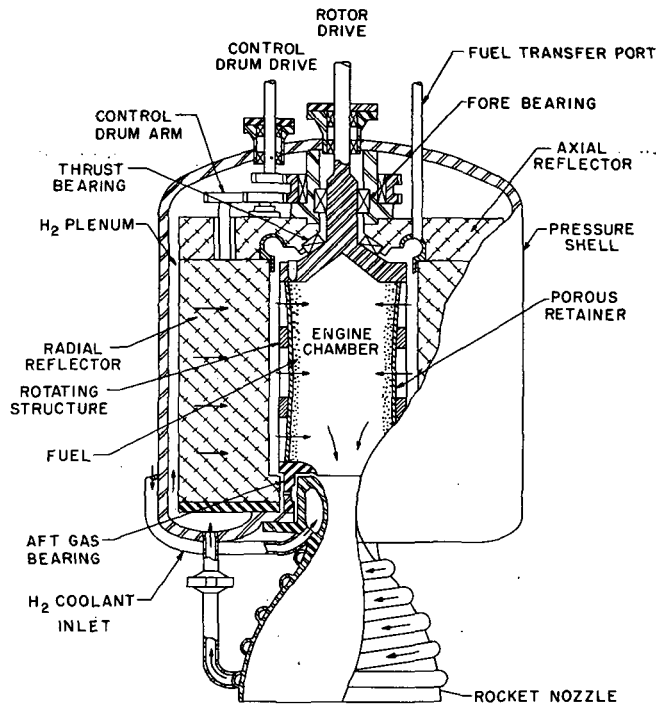


Figure 4 Rotating fluidized bed reactor

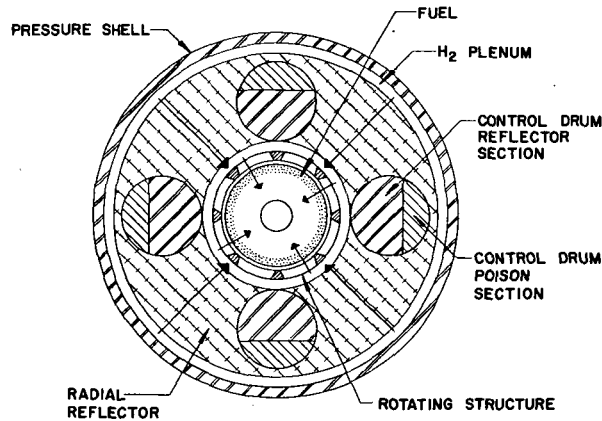


Figure 5 Section through rotating fluidized bed reactor

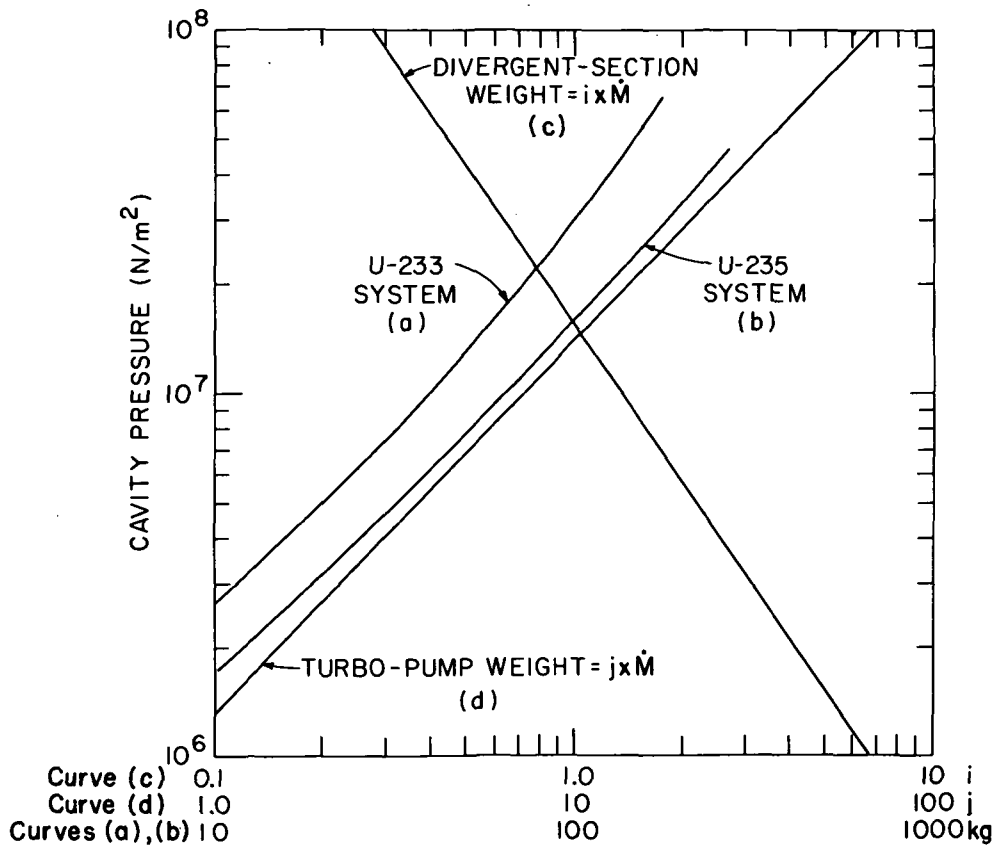


Figure 6 Graph of ^{235}U and ^{233}U system parameters

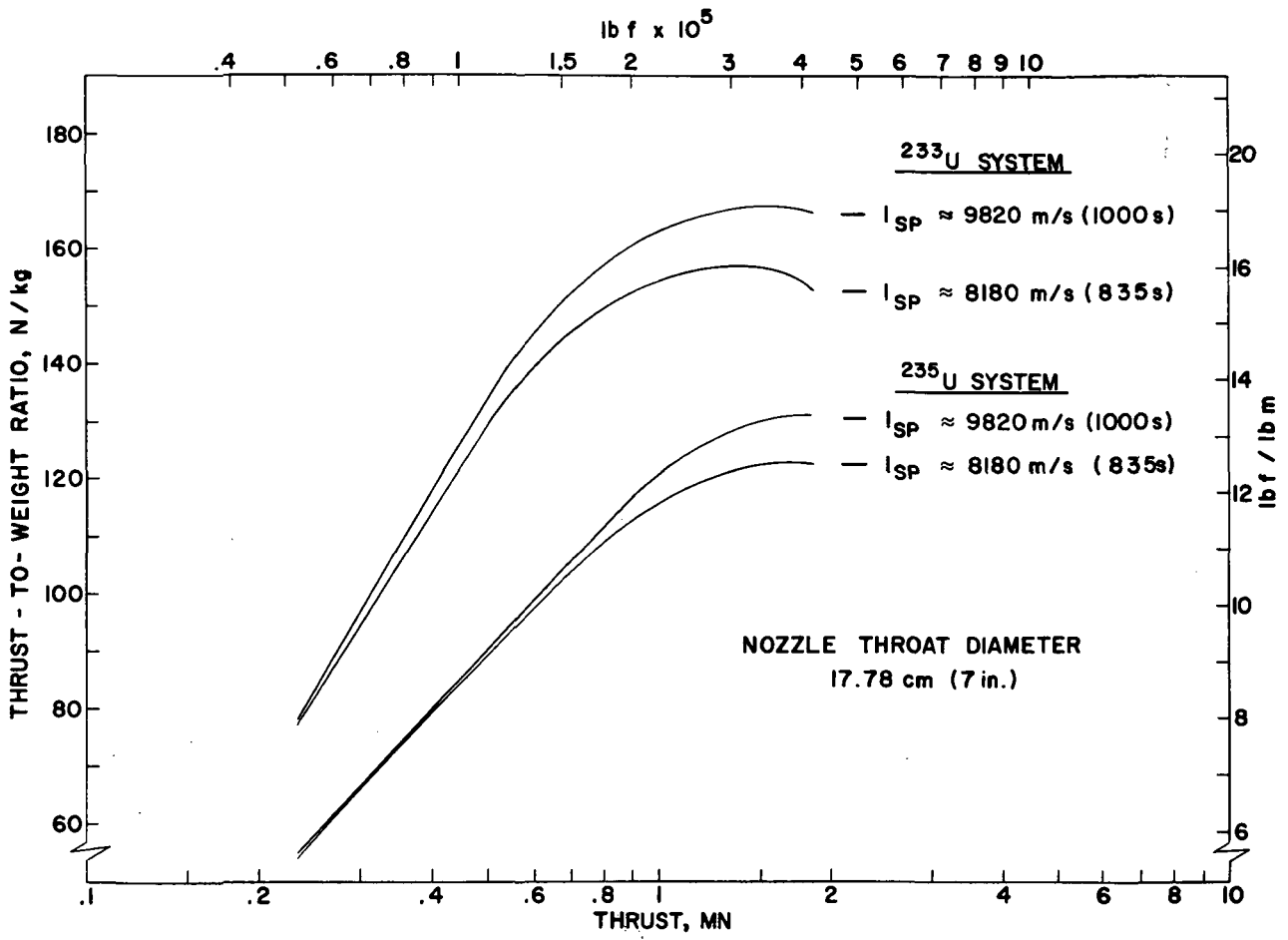


Figure 7 Variation of thrust-to-weight ratio with thrust

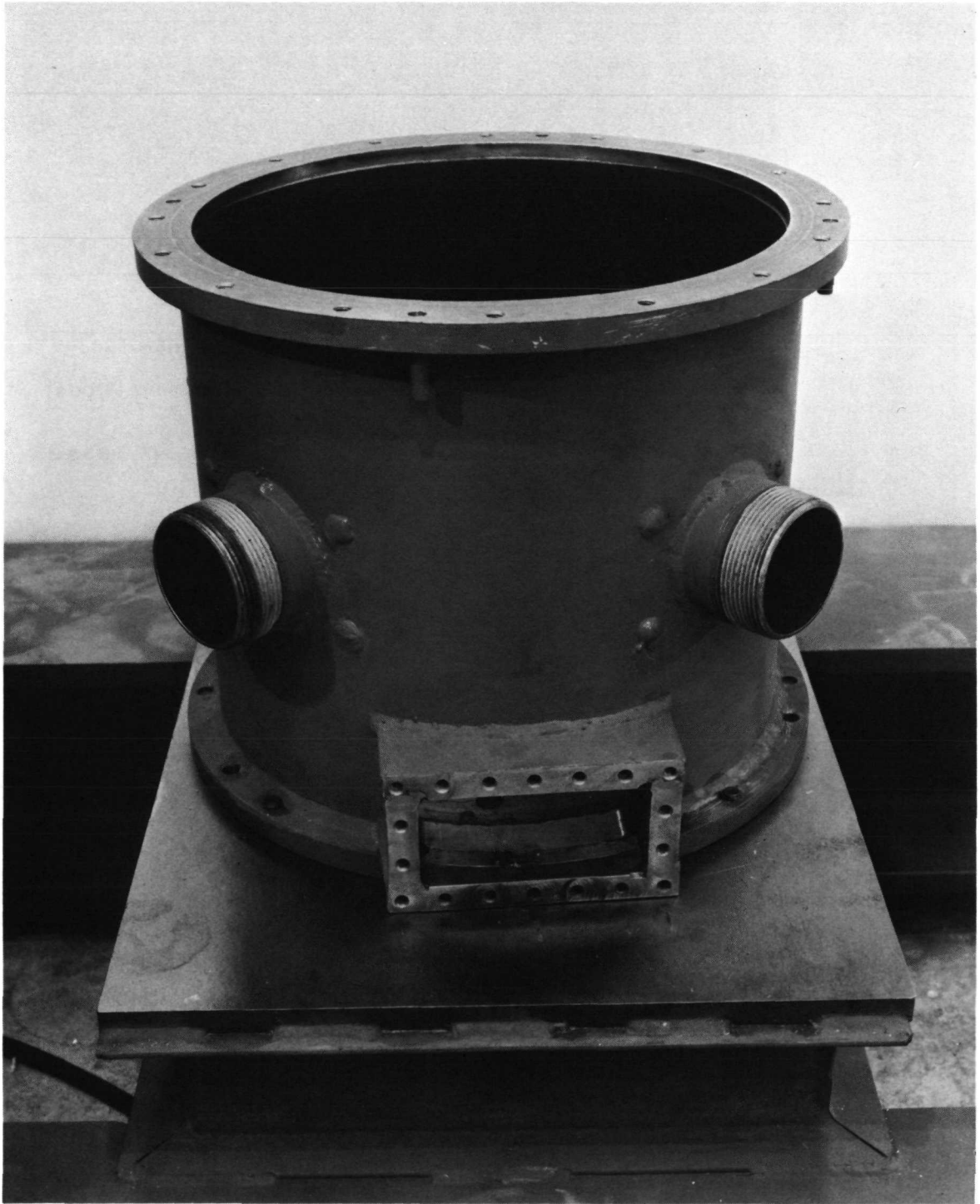


Figure 8 Gas distribution shell
showing two inlet ports
and photographic access
port

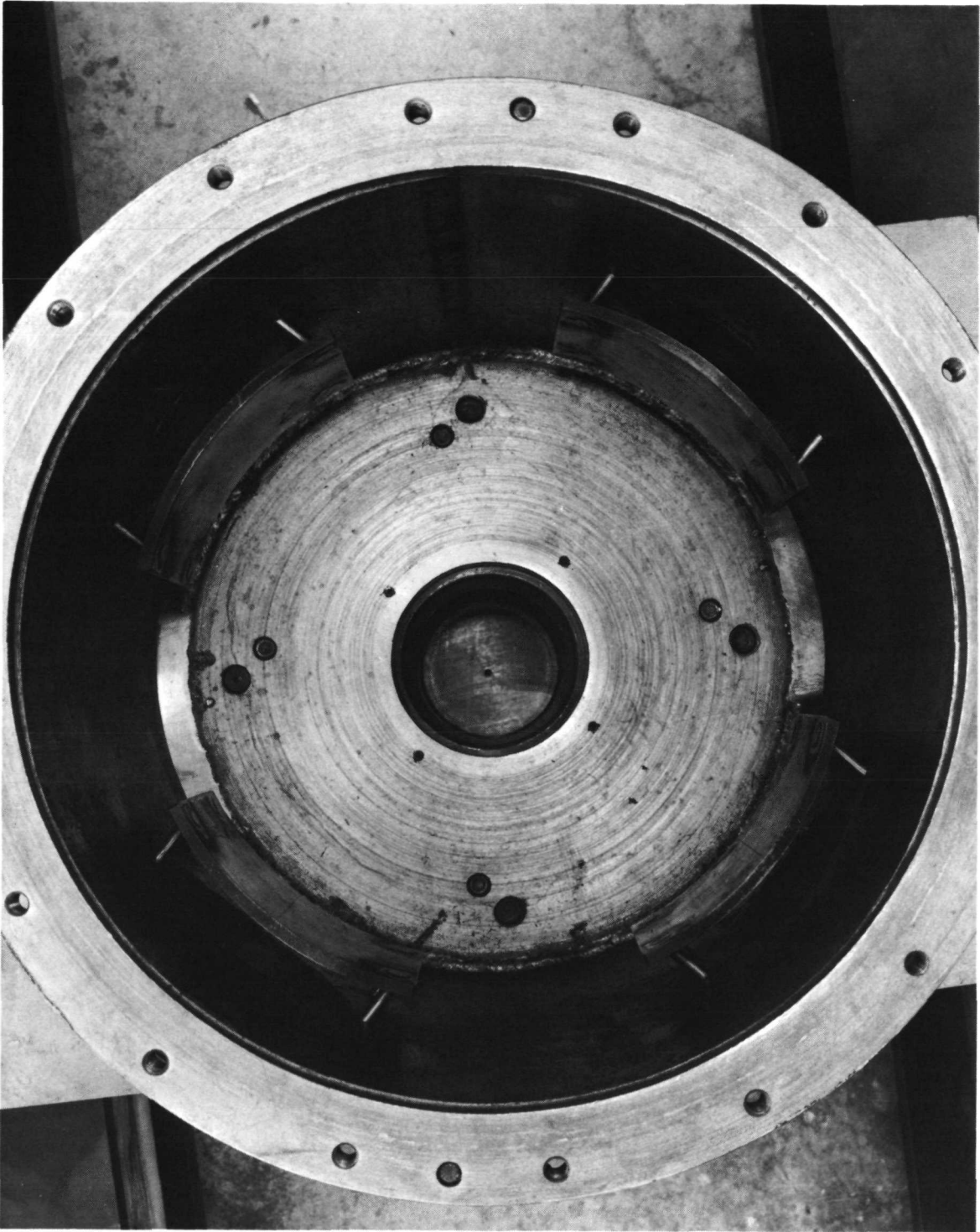


Figure 9 Inside view of shell showing gas distribution baffles



Figure 10 View of rotating drum showing perforated frit support

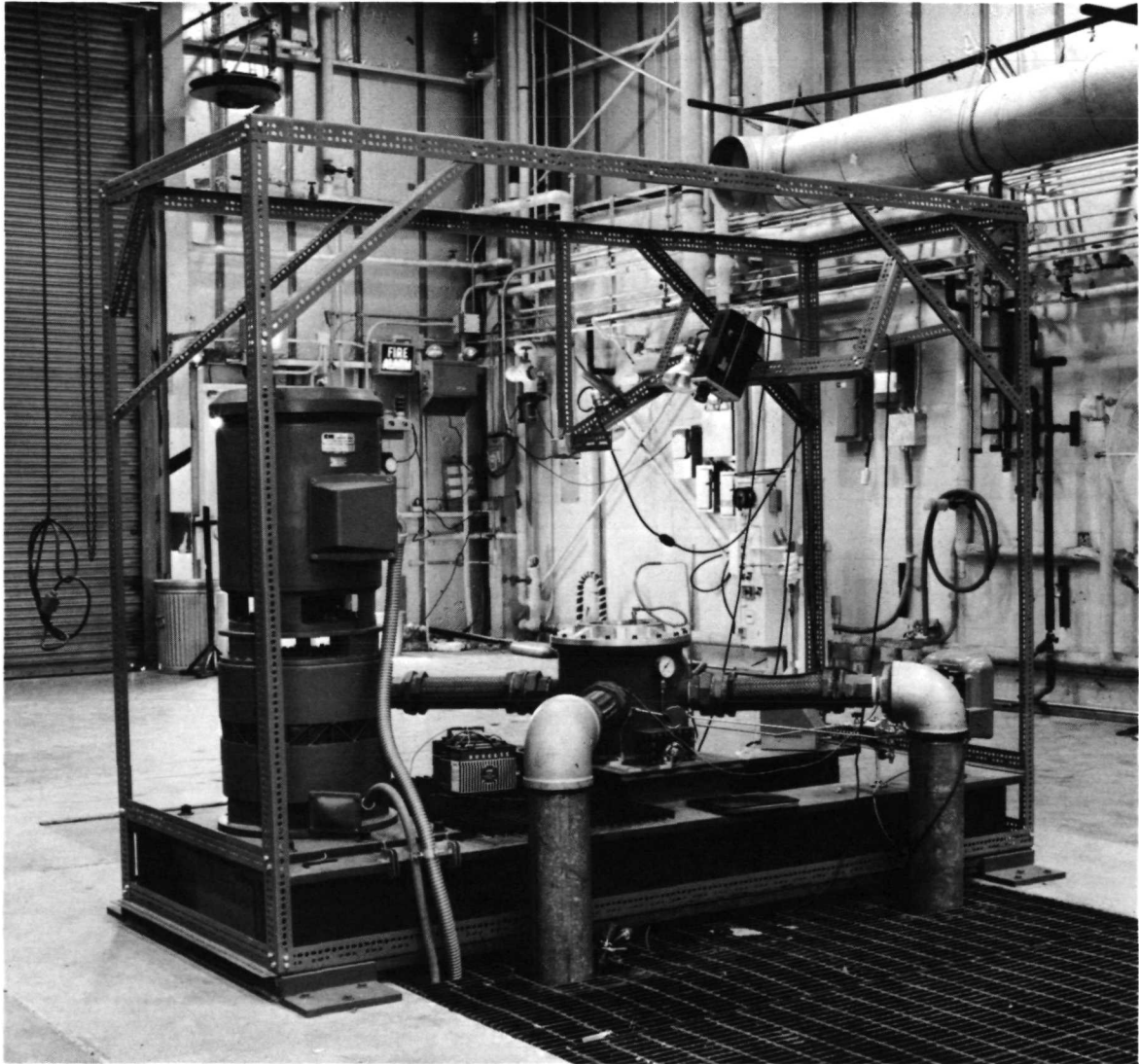


Figure 11 Rotating fluidized bed
assembly

C.2

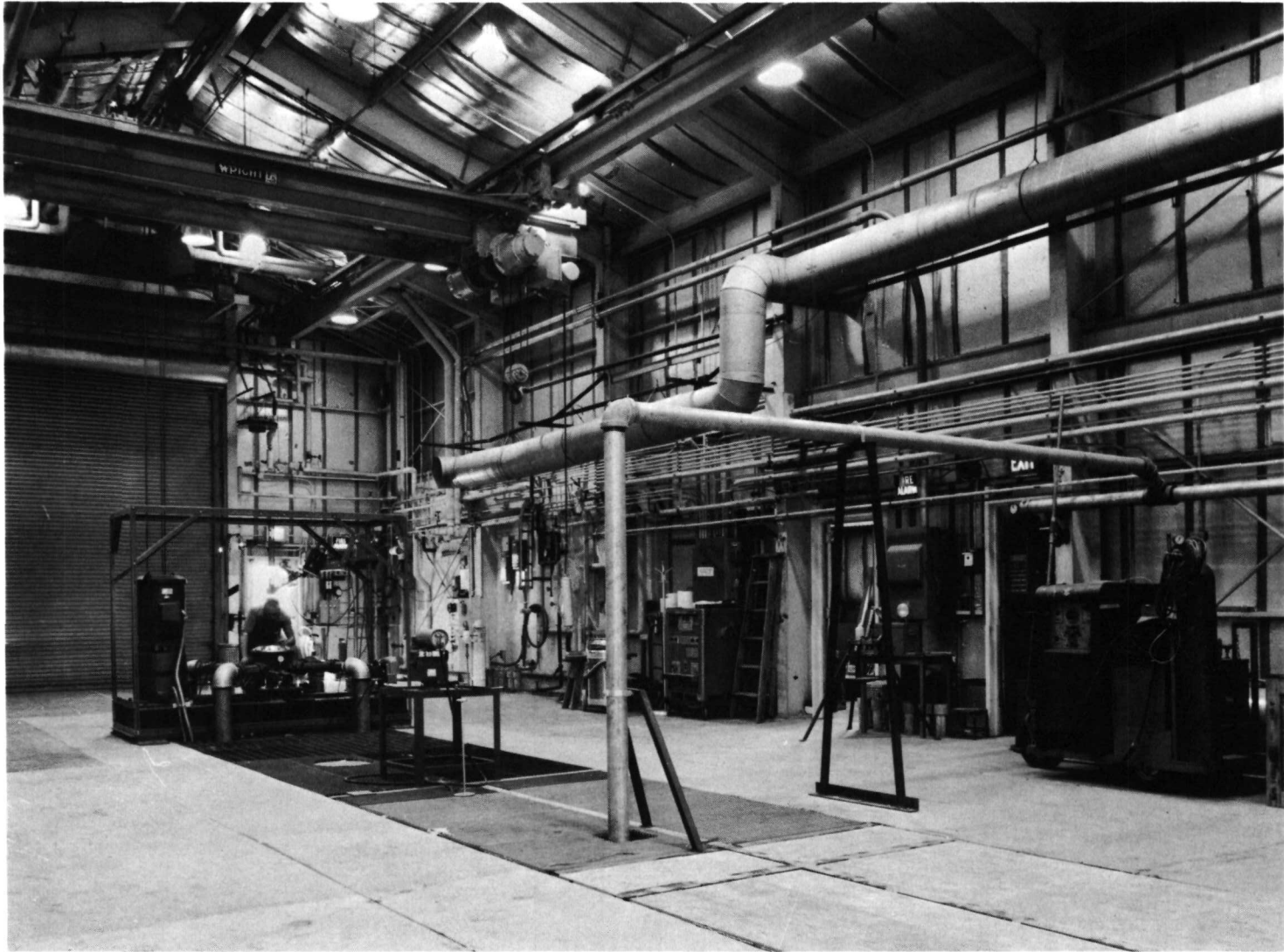


Figure 12 Experimental facility,
view from the east

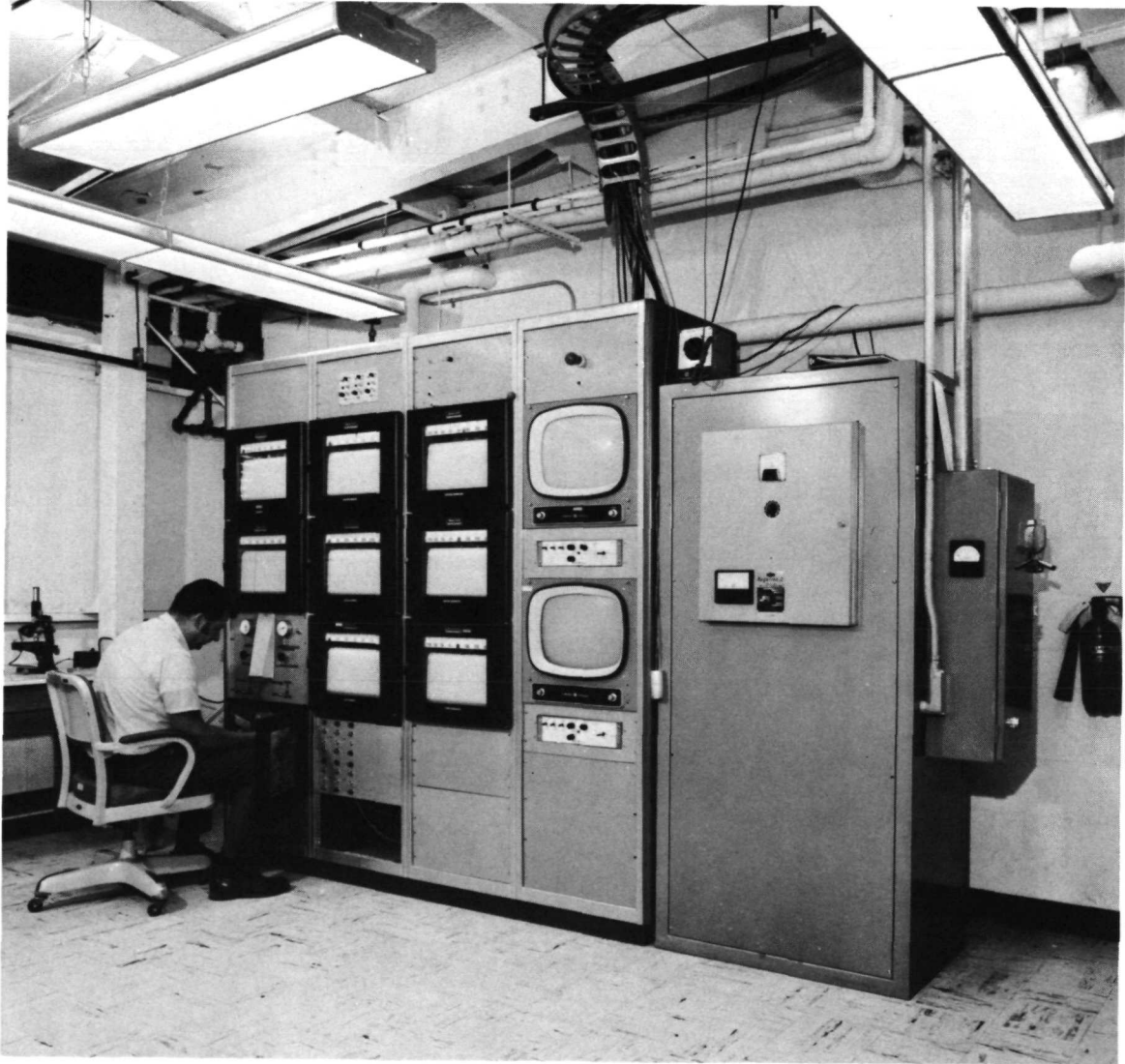
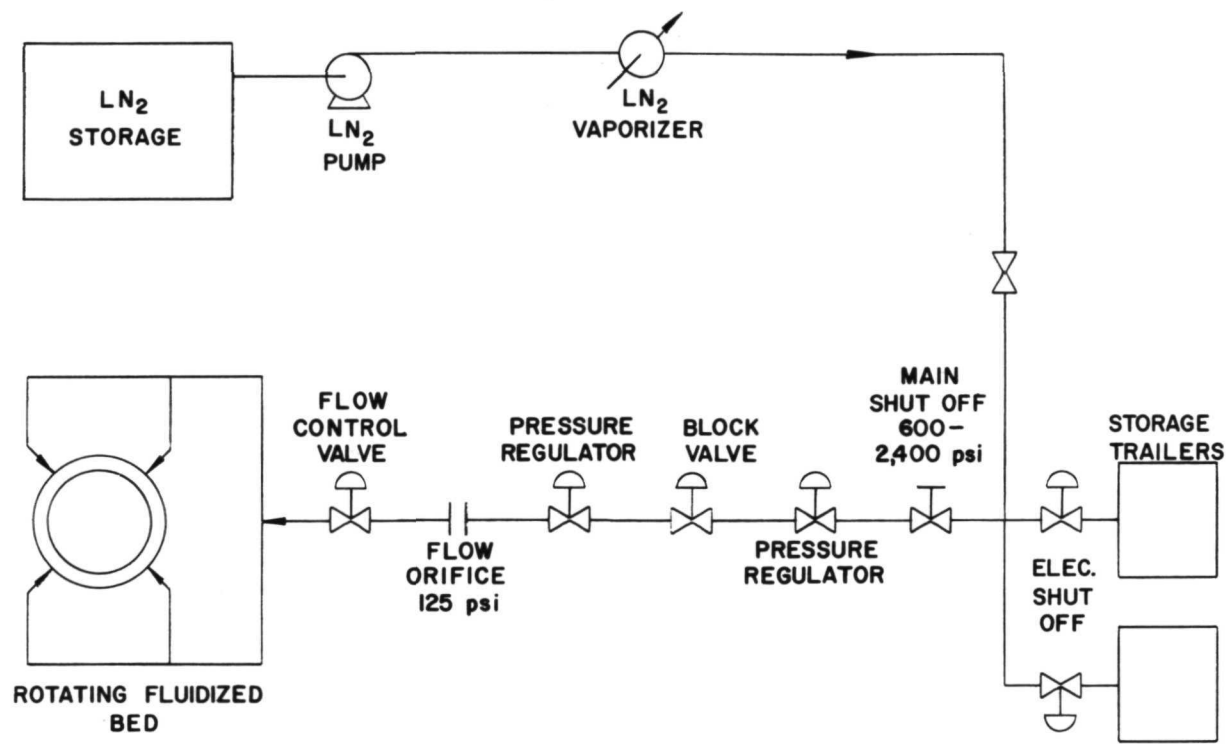


Figure 13 Control console



FLOW DIAGRAM

Figure 14 Flow diagram



Figure 15 6,800 liter LN₂ storage trailer

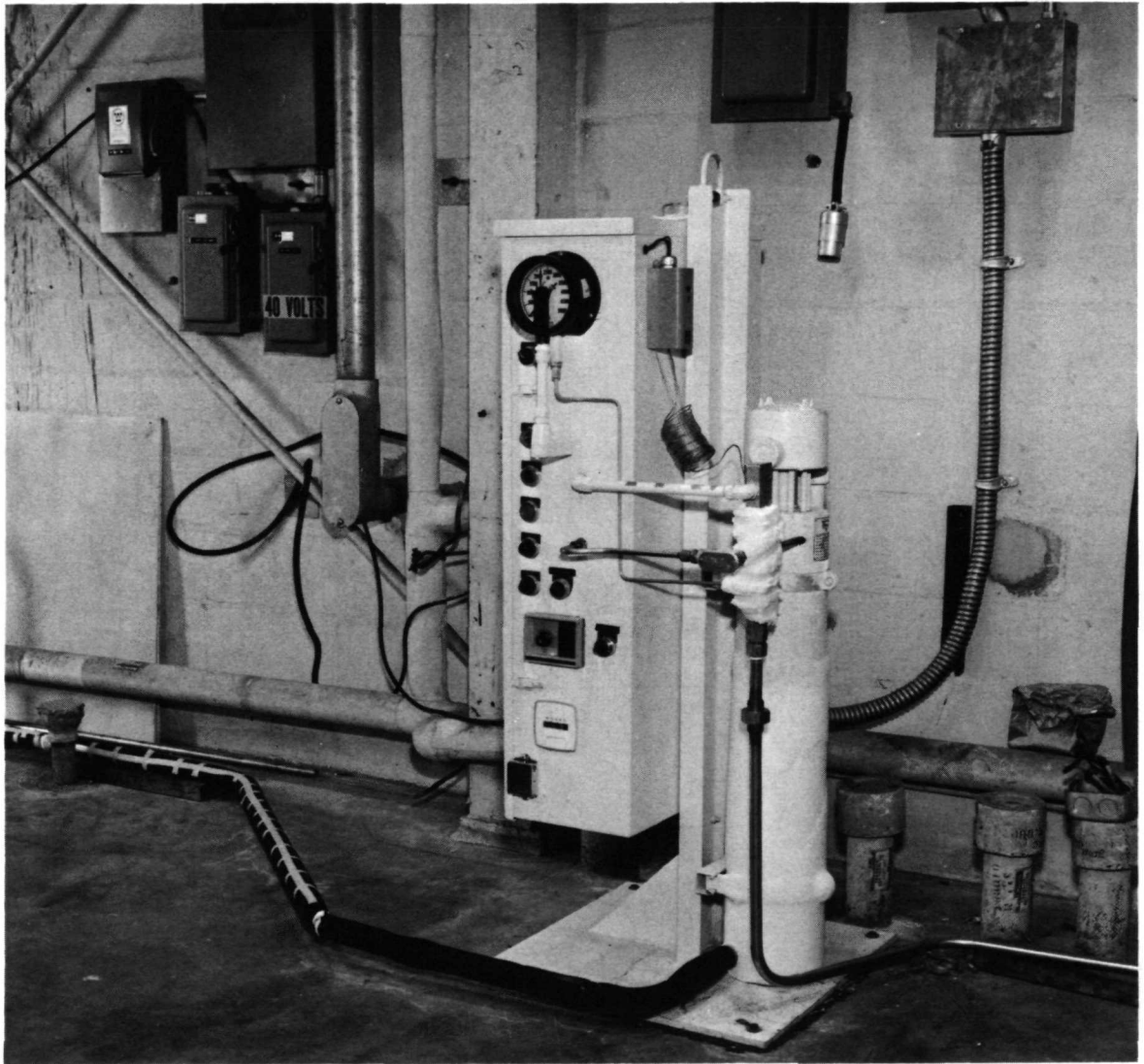


Figure 16 Liquid nitrogen vaporizer



Figure 17 High pressure nitrogen
gas storage trailers

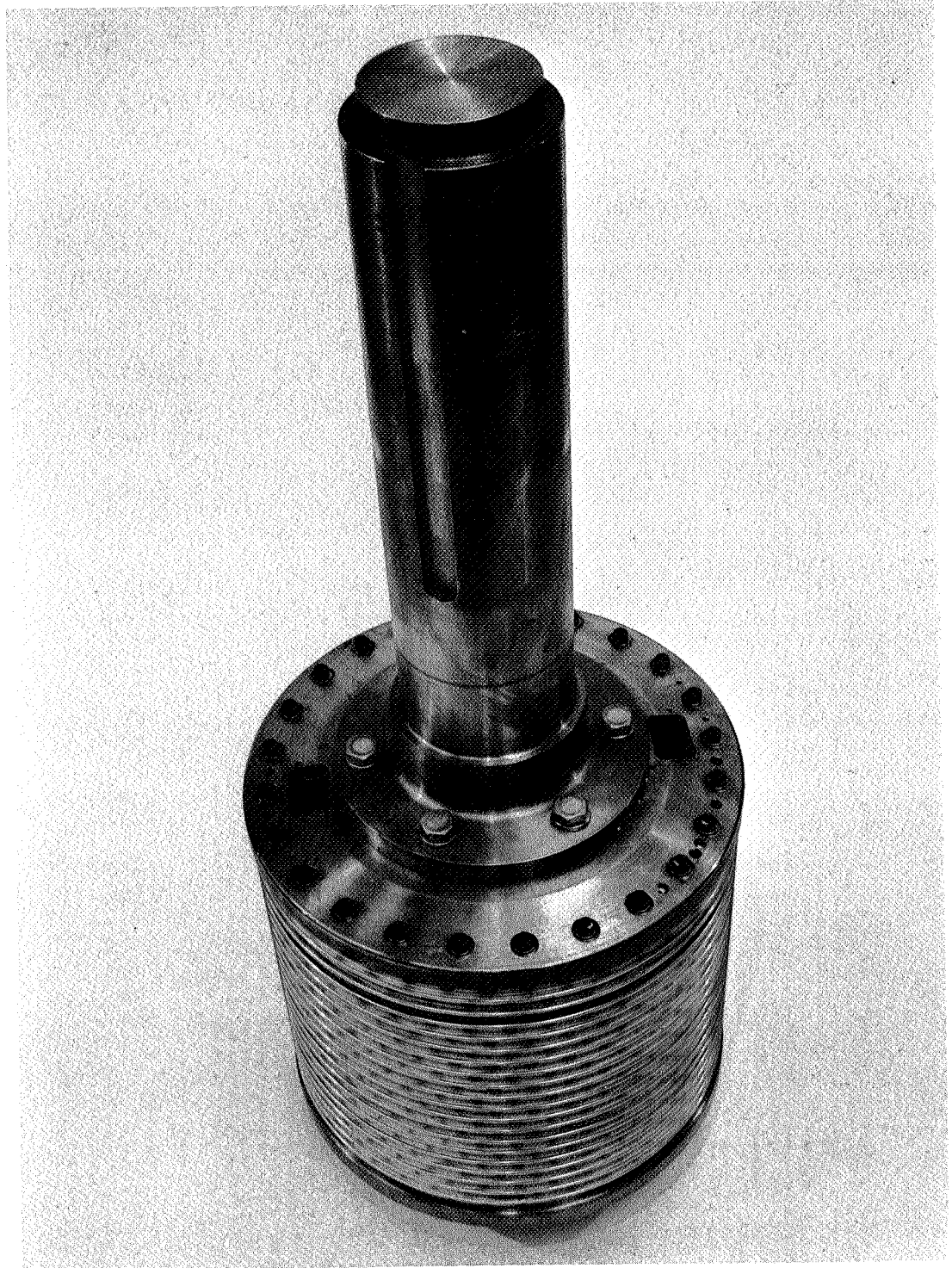


Figure 18a Bottom view of rotating
drum showing photo-
graphic viewing windows

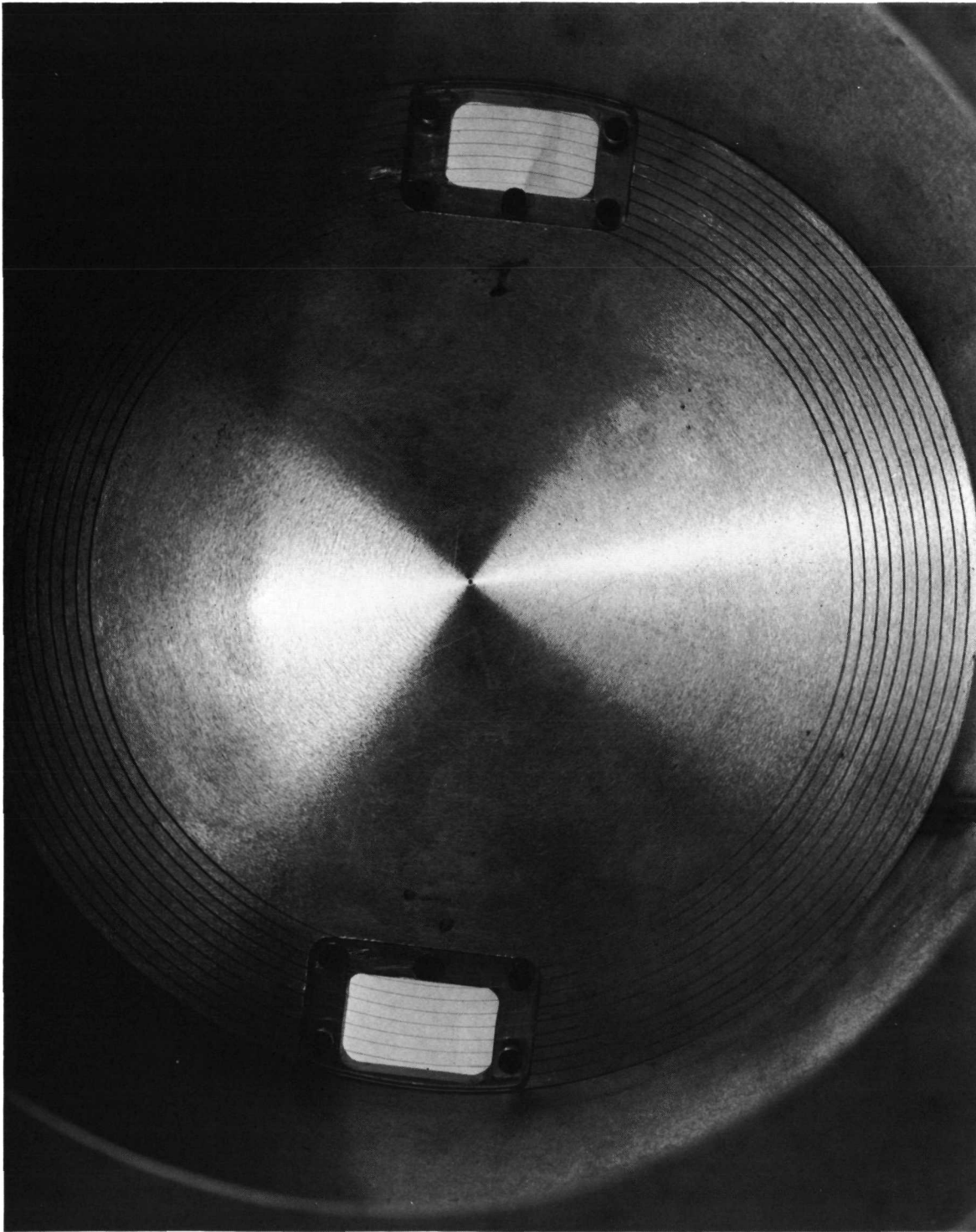


Figure 18b Inside view of rotating
drum showing grid lines
on viewing windows

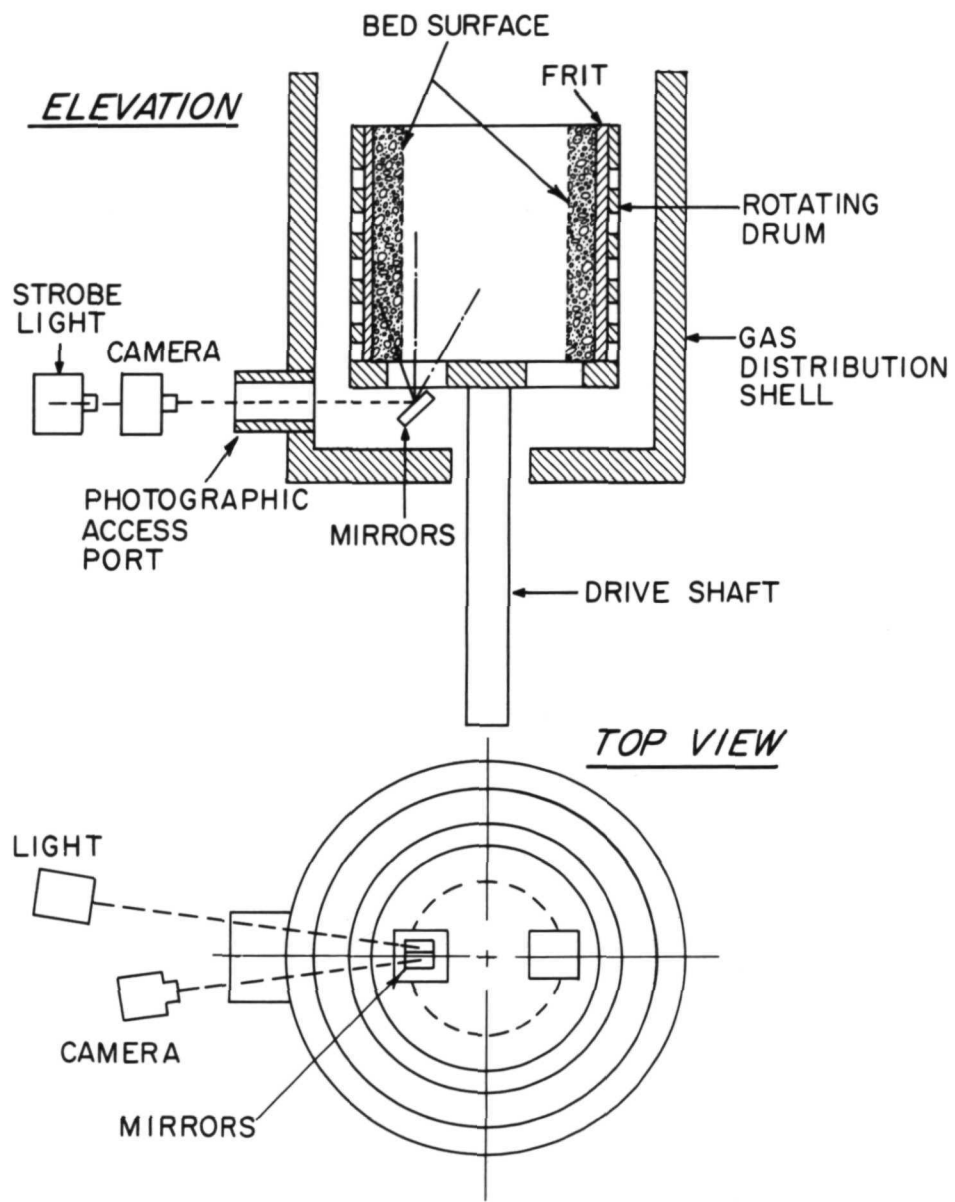


Figure 19 Schematic diagram of photographic system



Figure 20 View of bed taken through
bottom plate, Series 1-1
100 μ glass, 1,000 rpm,
0 m³/min

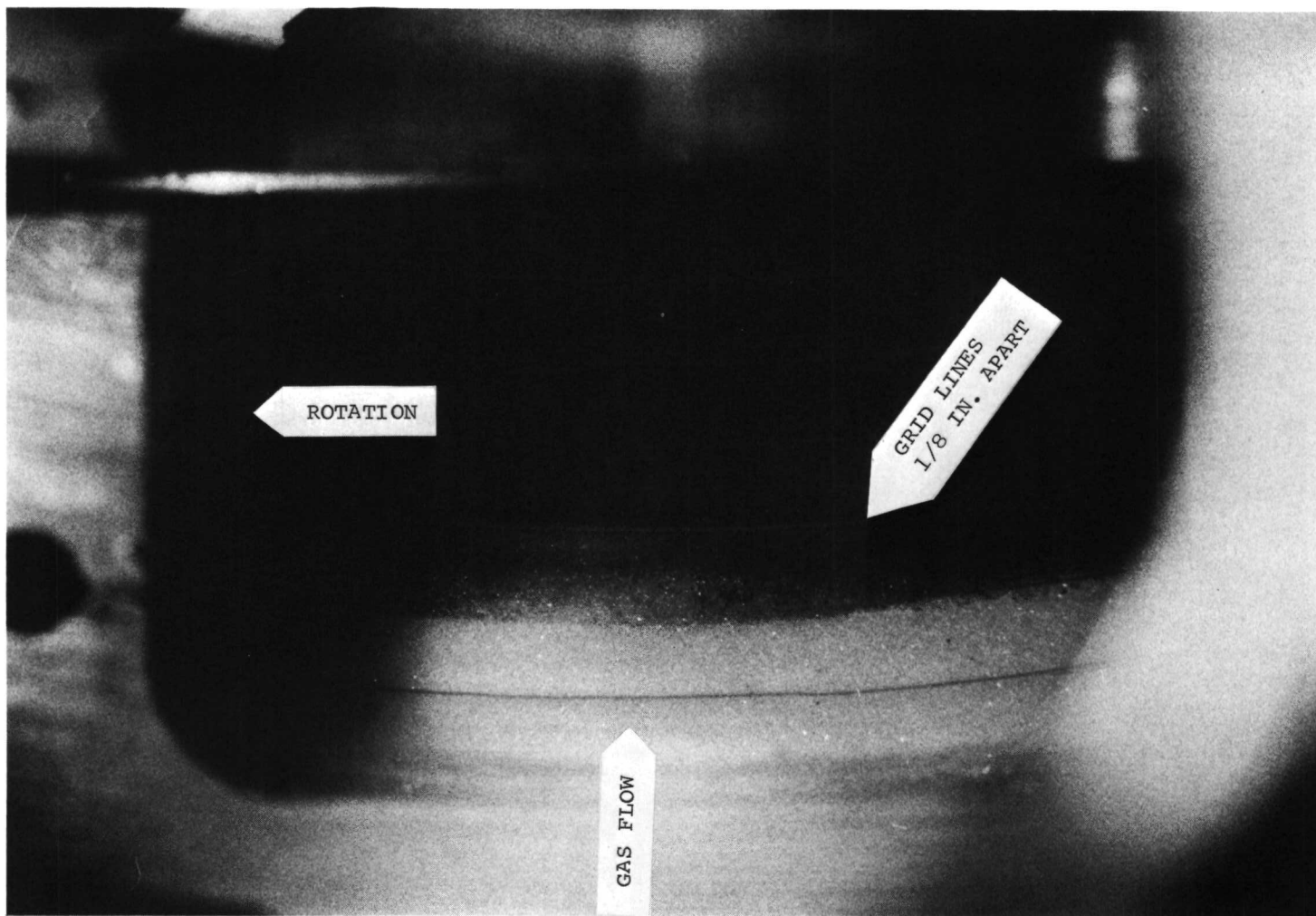


Figure 21 View of bed taken through
bottom plate, Series 1-2
100 μ glass, 1,000 rpm,
38 m³/min



Figure 22 View of bed taken through
bottom plate, Series 1-3
100 μ glass, 1,000 rpm,
45 m³/min



Figure 23 View of bed taken through
bottom plate, Series 1-4
100 μ glass, 1,000 rpm,
51 m³/min



Figure 24 View of bed taken from
bottom plate, Series 2-1
100 μ glass, 2,000 rpm,
0 m³/min

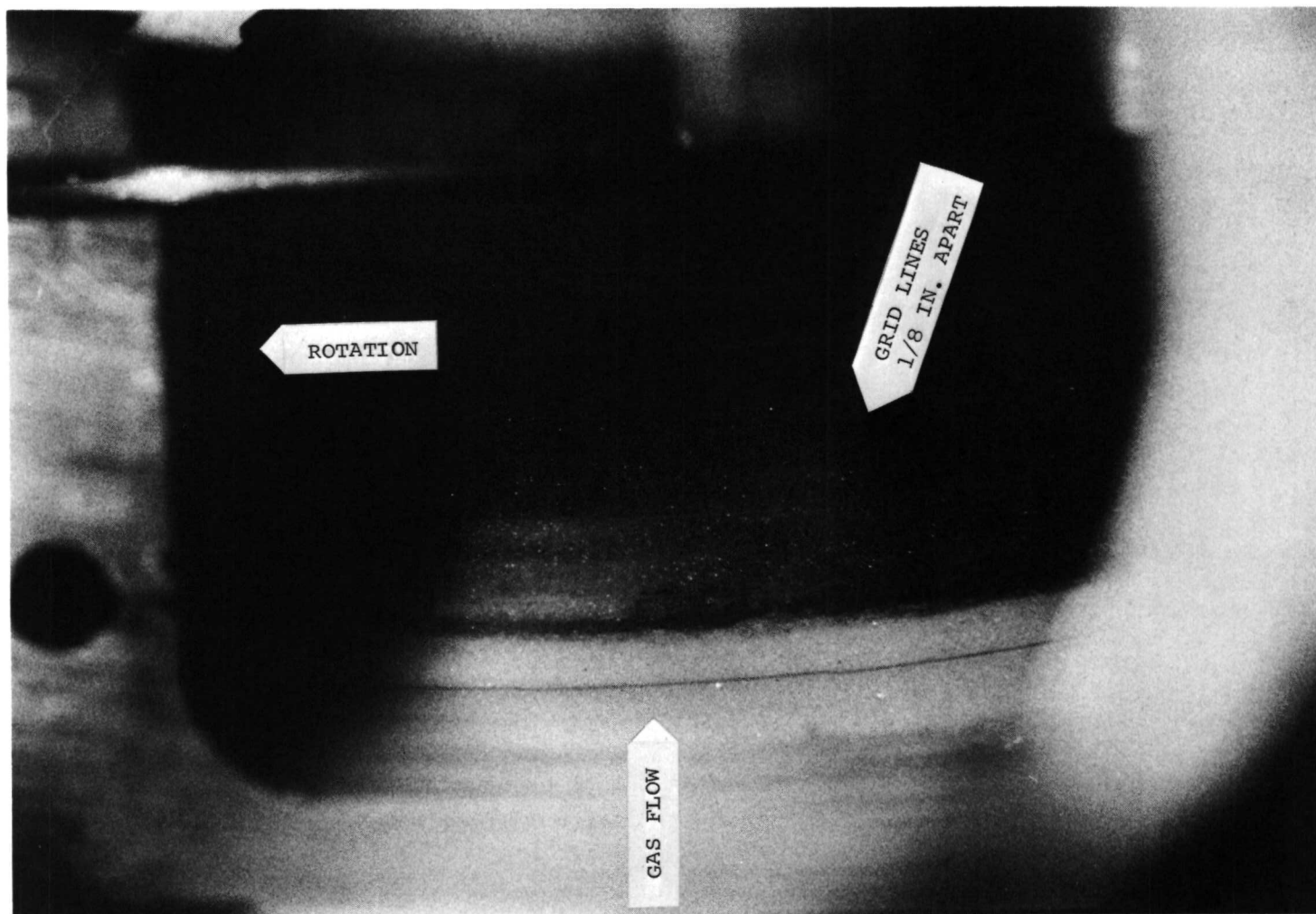


Figure 25 View of bed taken from
bottom plate, Series 2-2
100 μ glass, 2,000 rpm,
63 m³/min

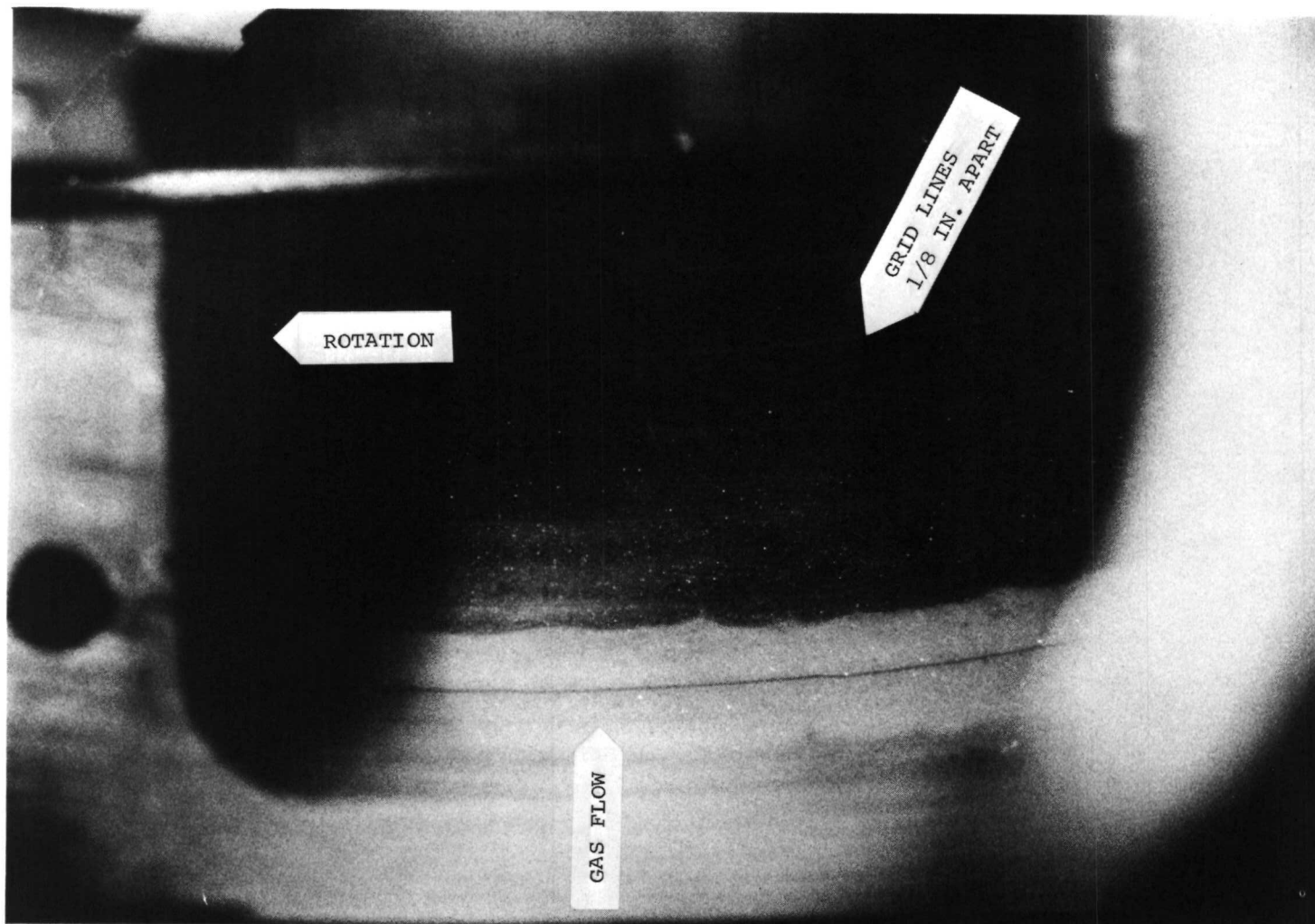


Figure 26 View of bed taken from
bottom plate, Series 2-3
100 μ glass, 2,000 rpm,
74 m³/min

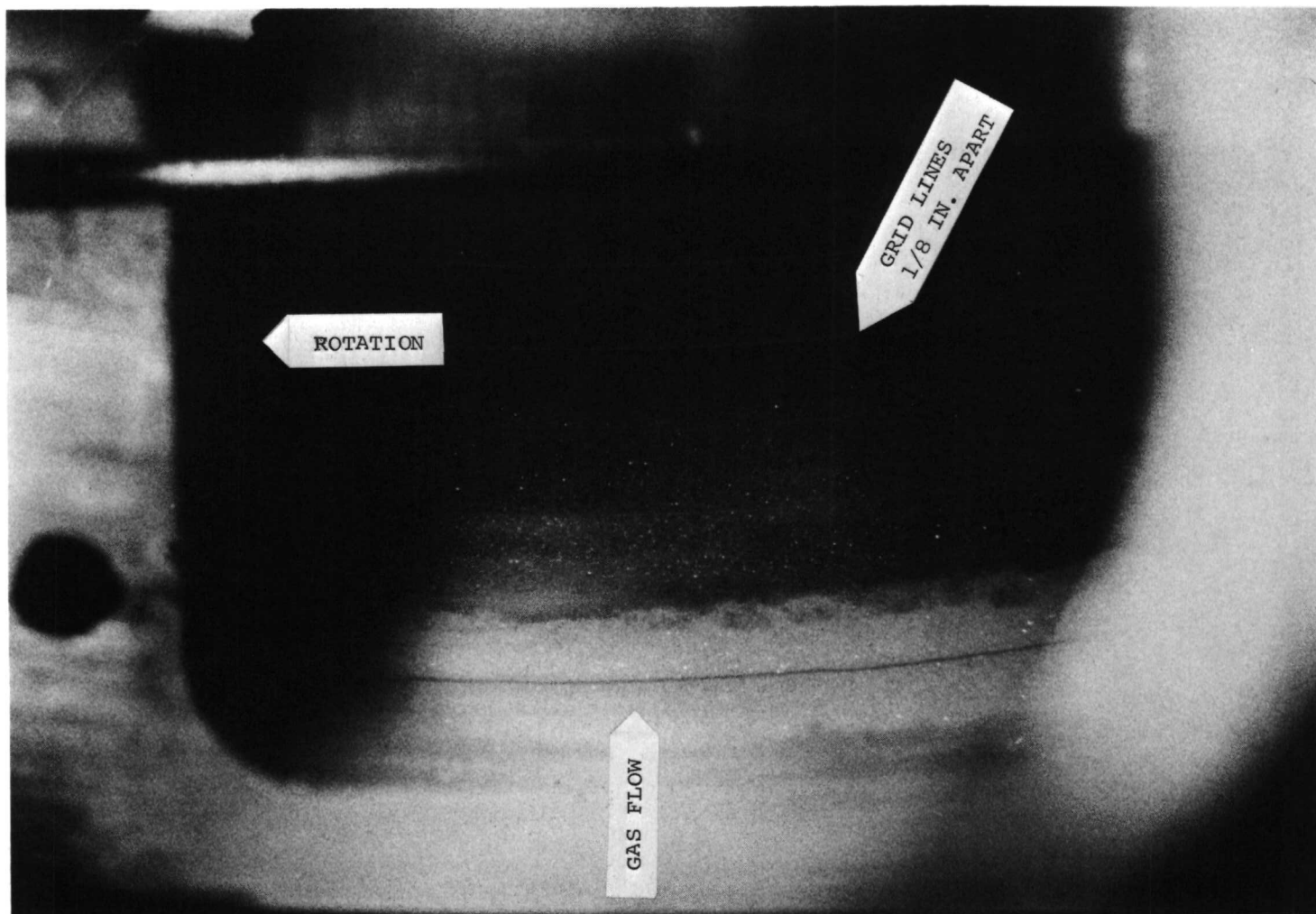


Figure 27 View of bed taken from
bottom plate, Series 2-4
100 μ glass, 2,000 rpm,
82 m^3/min



Figure 28 View of bed taken through
bottom plate, Series 3-1
500 μ glass, 1,000 rpm,
0 m^3/min

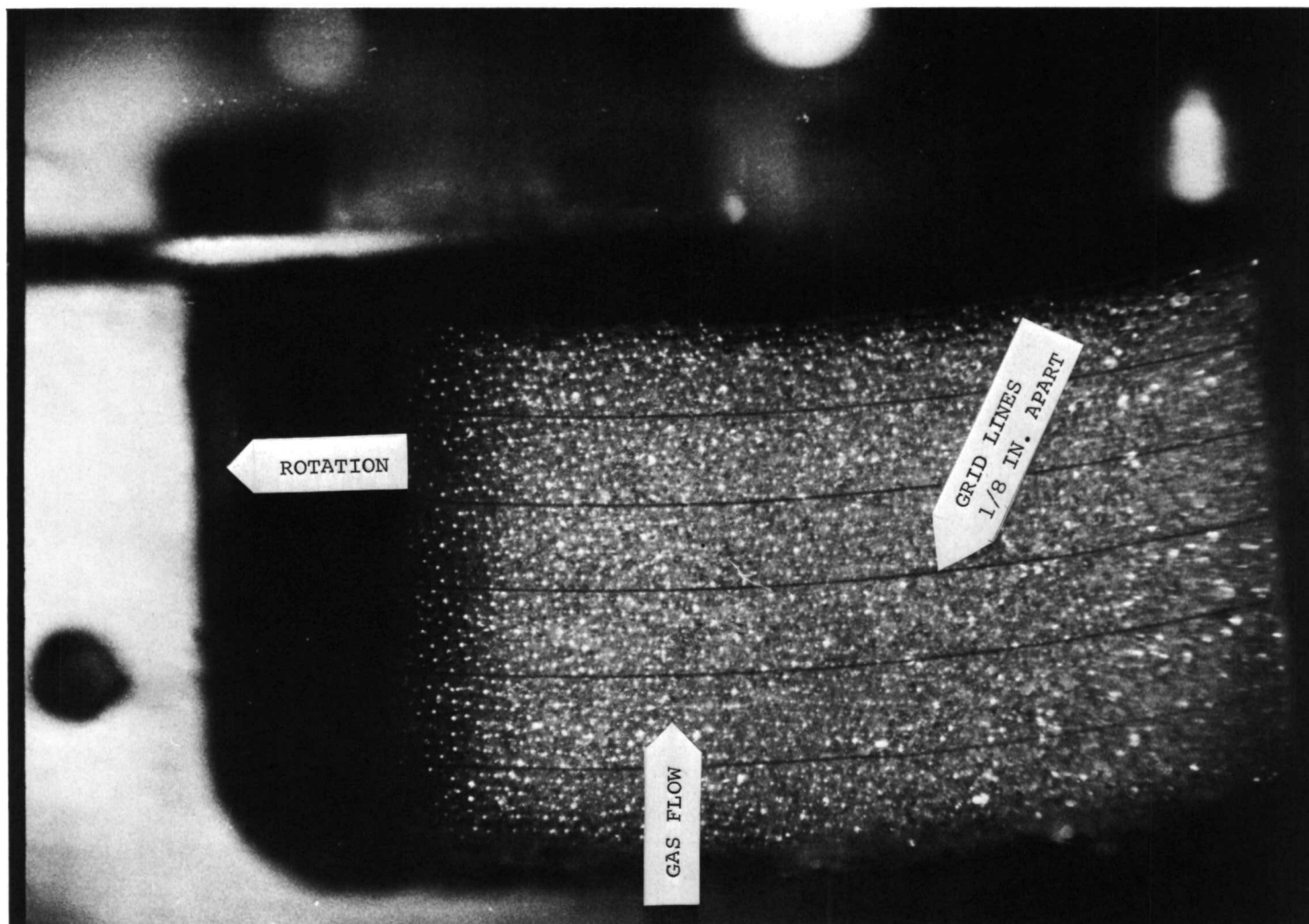


Figure 29 View of bed taken through
bottom plate, Series 3-2
500 μ glass, 1,000 rpm,
85 m³/min

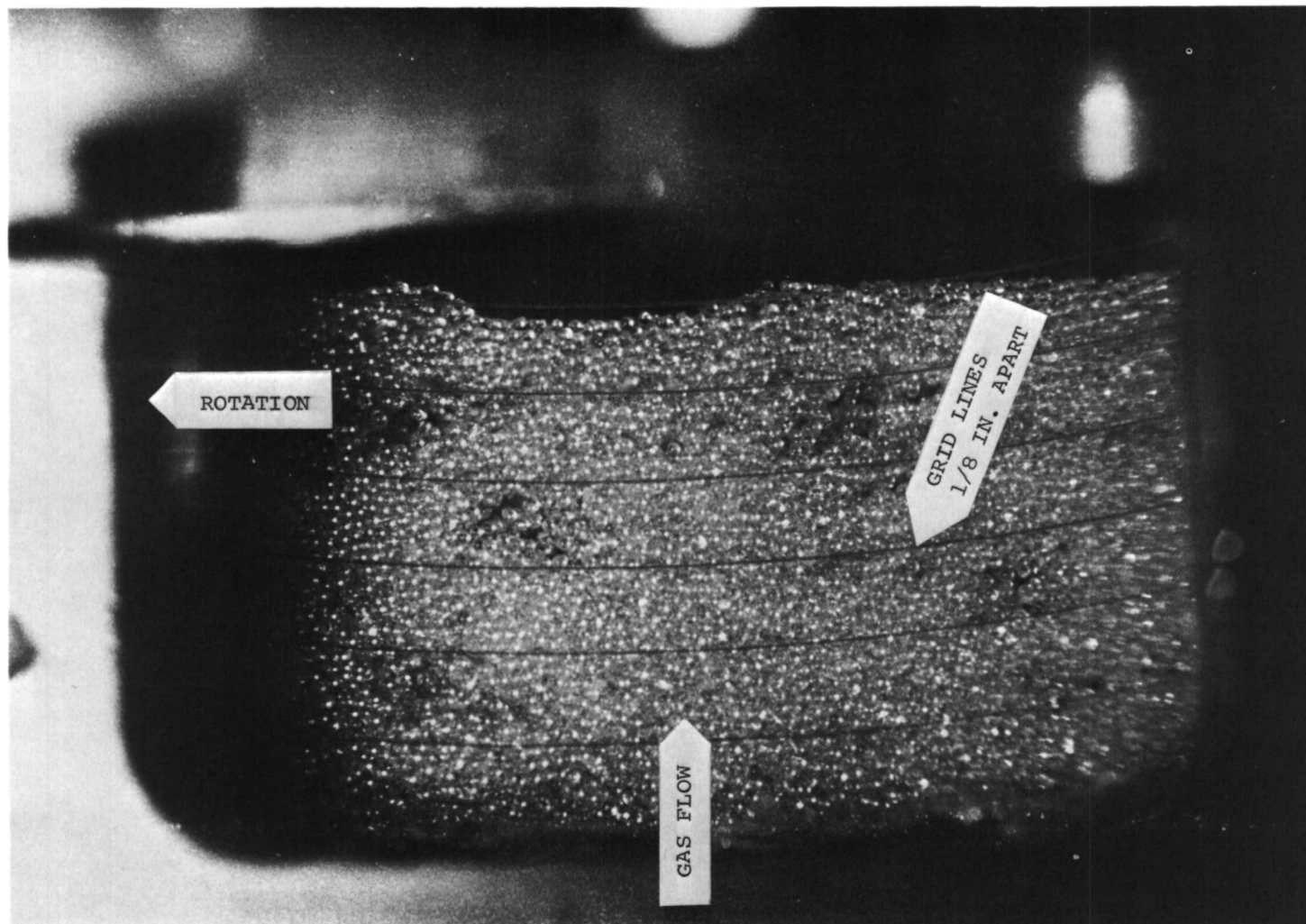


Figure 30 View of bed taken through
bottom plate, Series 3-3
500 μ glass, 1,000 rpm,
170 m^3/min

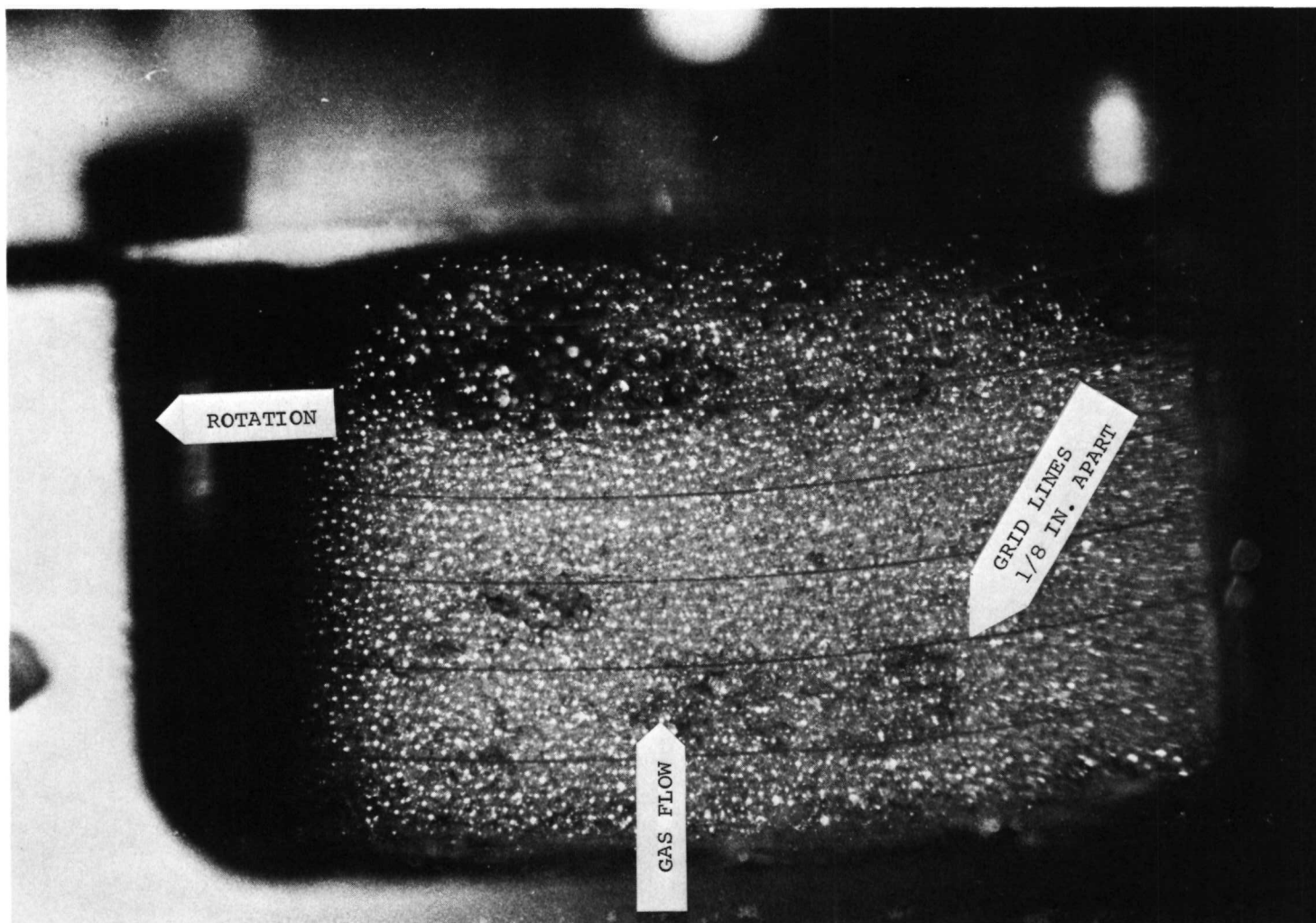


Figure 31 View of bed taken through
bottom plate, Series 3-4
500 μ glass, 1,000 rpm,
213 m^3/min



Figure 32 View of bed taken through
bottom plate, Series 4-1
500 μ glass, 2,000 rpm,
0 m³/min

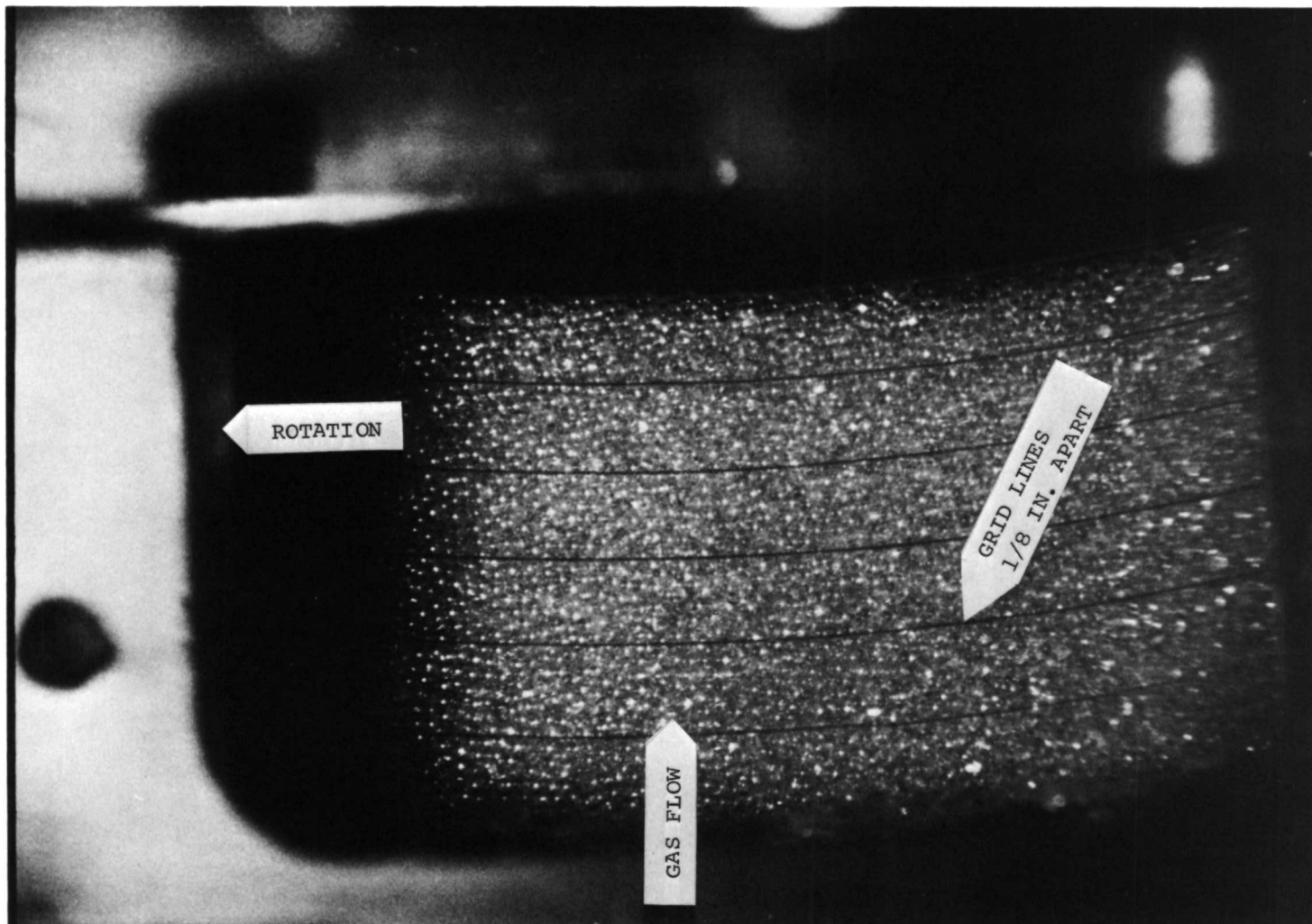


Figure 33 View of bed taken through
bottom plate, Series 4-2
500 μ glass, 2,000 rpm,
85 m^3/min

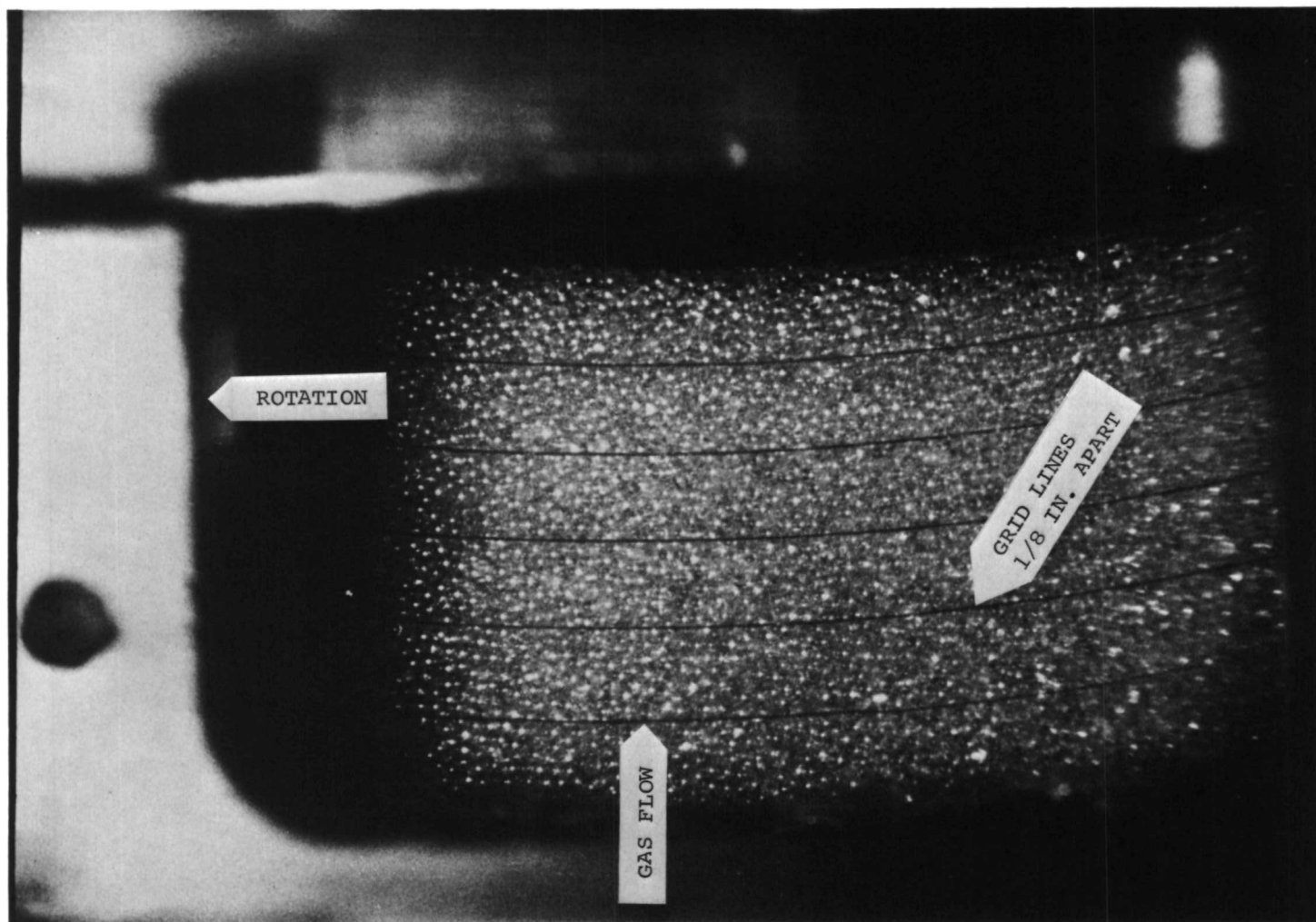


Figure 34 View of bed taken through
bottom plate, Series 4-3
500 μ glass, 2,000 rpm,
170 m^3/min



Figure 35 View of bed taken through
bottom plate, Series 5-1
500 μ copper, 700 rpm,
0 m³/min

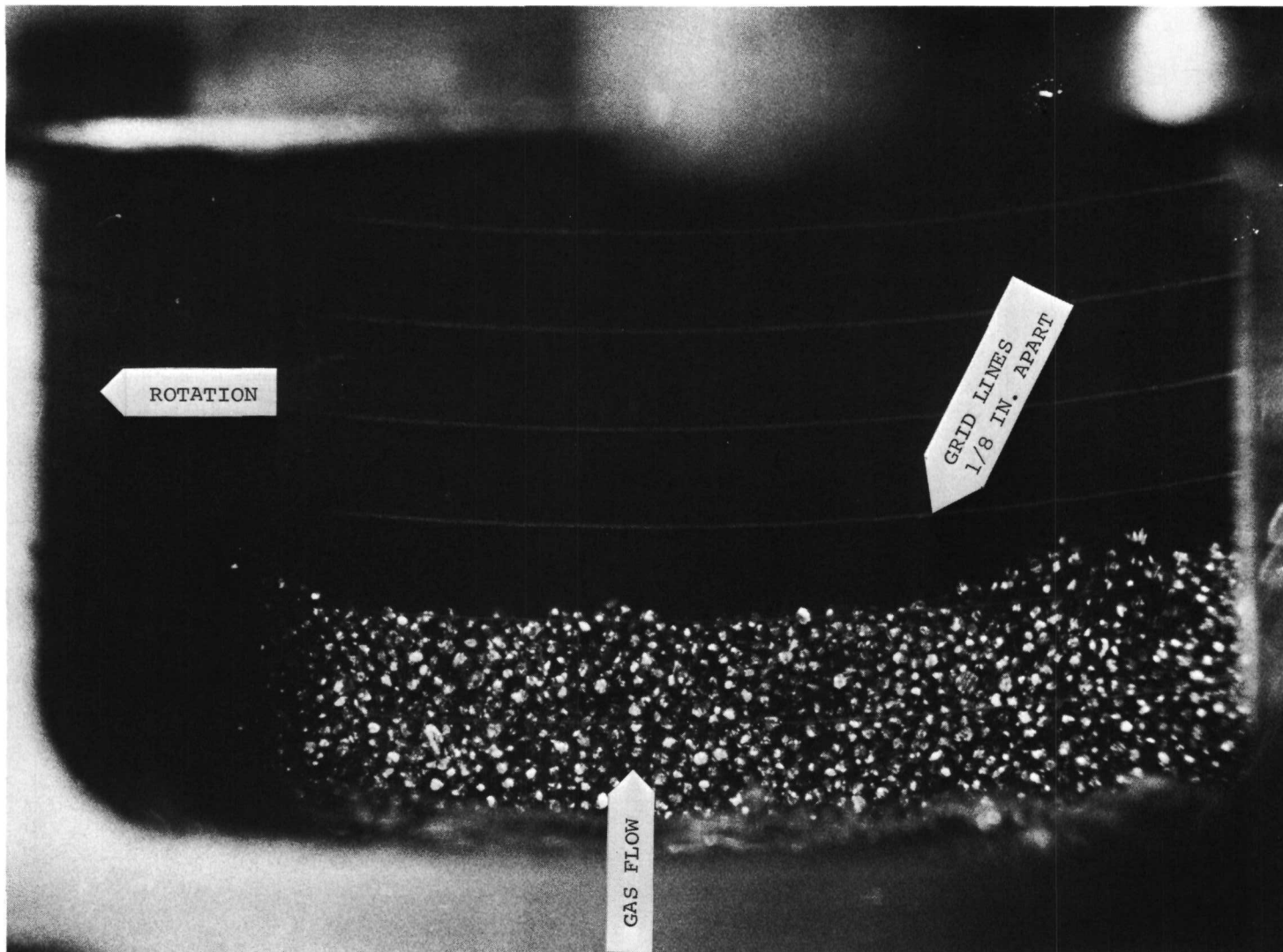


Figure 36 View of bed taken through
bottom plate, Series 5-2
500 μ copper, 700 rpm,
170 m^3/min



Figure 37 View of bed taken through
bottom plate, Series 5-3
500 μ copper, 700 rpm,
232 m^3/min

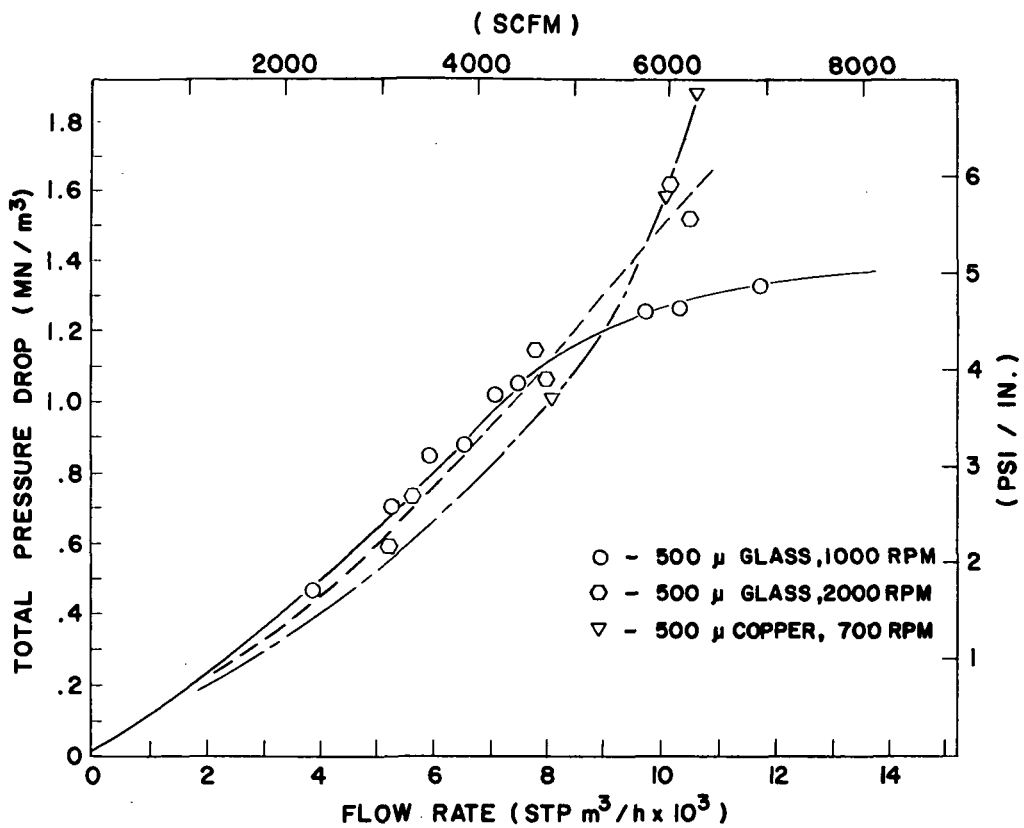


Figure 38 Total pressure drop per unit bed thickness as a function of flow rate

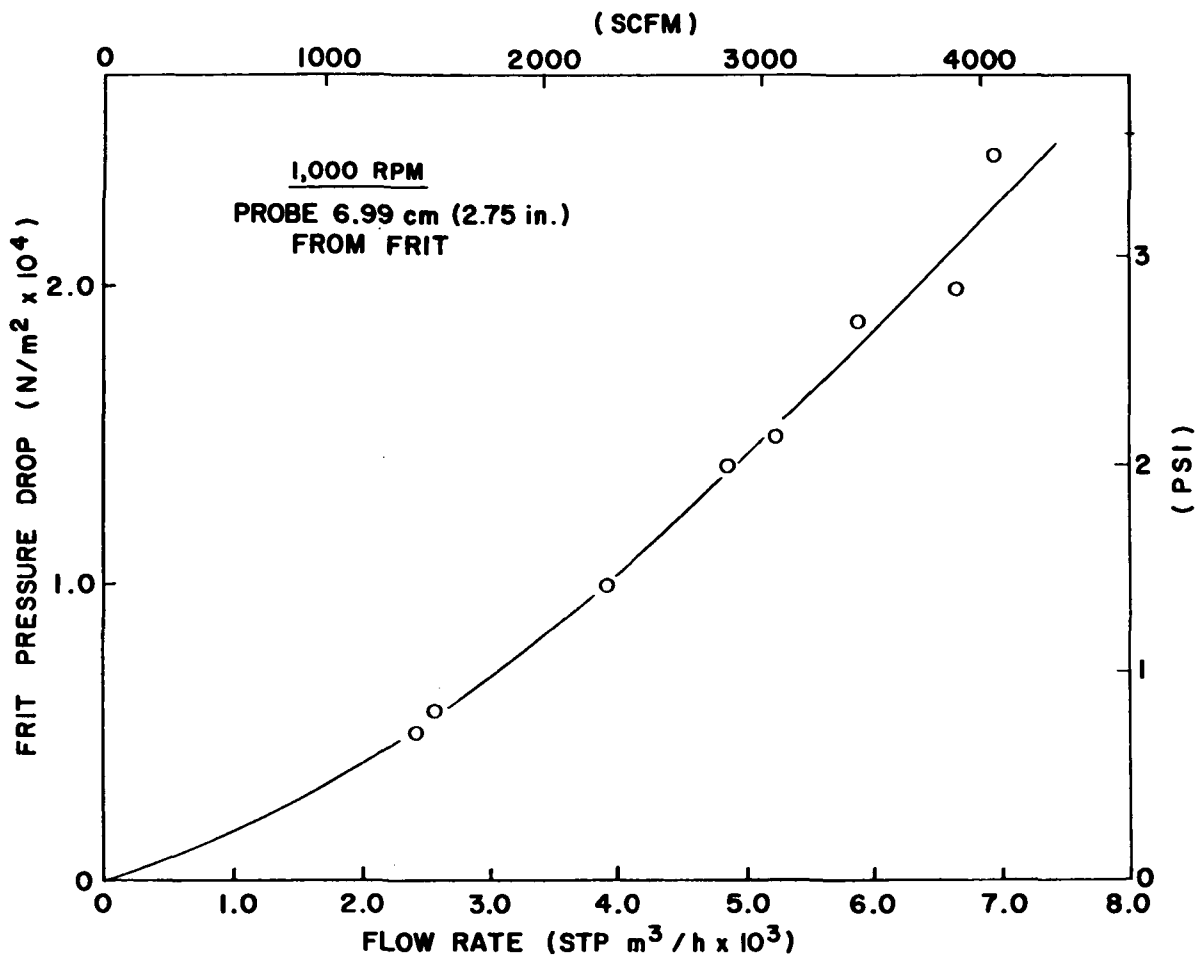


Figure 39 Frit pressure drop as a function of flow rate (1,000 rpm)

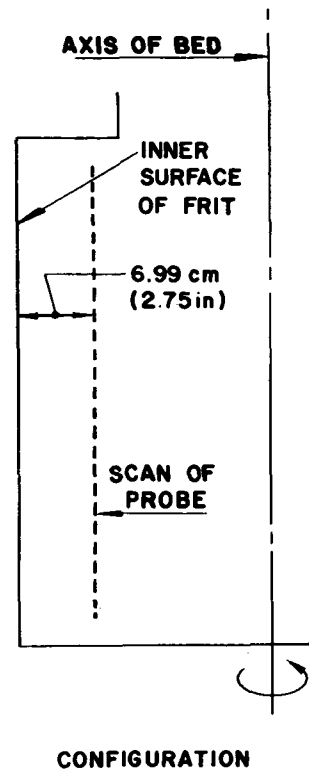
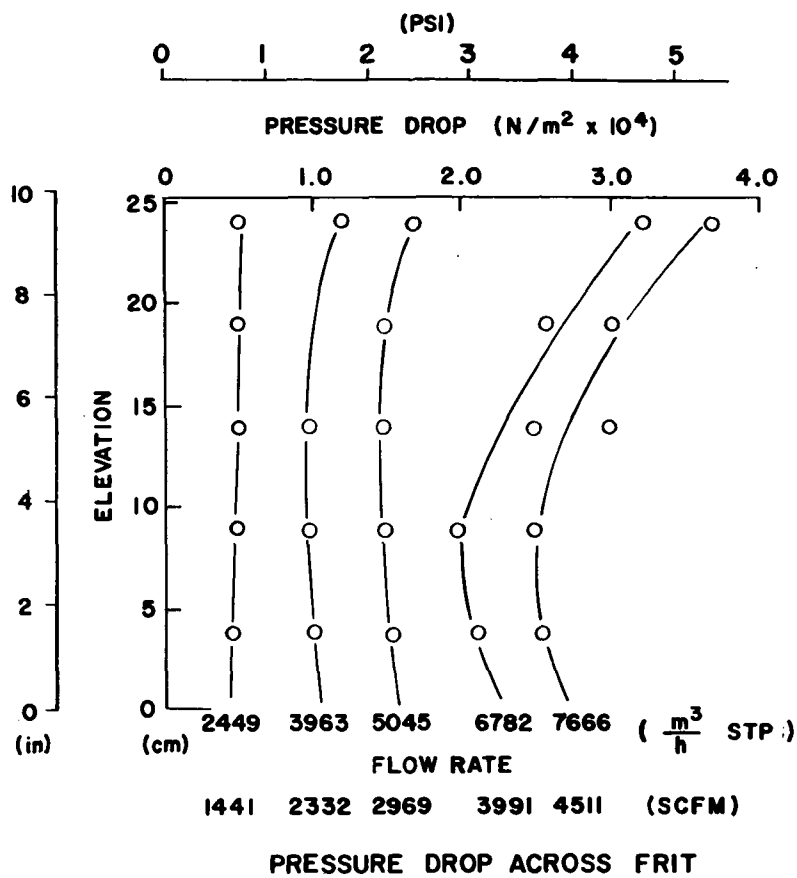
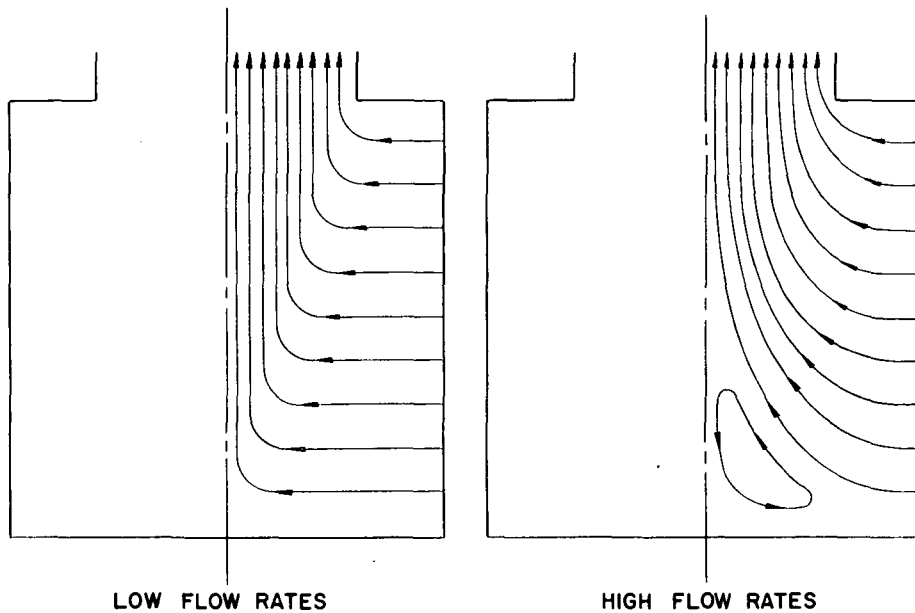


Figure 40 Effect of distance from closed end of bowl on pressure drop



LOW FLOW RATES

HIGH FLOW RATES

FLOW STREAMLINES

Figure 41 Flow streamlines in bowl